Vibration Suppression Using Smart Materials in the Presence of Temperature Changes

Thomas Hegewald

Thesis submitted to the Faculty of
Virginia Polytechnic Institute and State University
in partial fulfillment of the requirements for the degree of

Master of Science
in
Mechanical Engineering

Daniel J. Inman, Chair
Mehdi Ahmadian
Donald J. Leo

July 19, 2000
Blacksburg, Virginia

Keywords: Structural Vibration, Positive Position Feedback (PPF), Auto-Tuning, Active Damping, Piezoceramics, Smart Damping Materials.

Vibration Suppression Using Smart Materials in the Presence of Temperature Changes

Thomas Hegewald

(Abstract)

Aircraft and satellite structures are exposed to a wide range of temperatures during normal operation cycles. These fluctuations in temperature may result in significant changes of the structural dynamics. Aircraft, automotive, and satellite structures are also subject to various vibration sources. Passive and active vibration suppression techniques have been developed to minimize acoustic noise and fatigue stress damage. Featuring low weight solutions and high performance, active control techniques are becoming increasingly common. Structures with varying dynamics require more sophisticated active control techniques, such as adaptive control.

This research uses a special vibration test rig for evaluating the performance of different vibration suppression systems on a representative aircraft panel. The test panel is clamped rigidly in a frame and can be excited in various frequencies with an electromagnetic shaker. To simulate temperature fluctuations the temperature on the panel can be increased up to 65°C (150°F). Smart material based sensors and actuators are used to interface the mechanical system with the electronic controller. The active controller utilizes three positive position feedback (PPF) filters implemented through a digital signal processor board. This research develops two different adaptation methods to perform vibration suppression in the presence of thermally induced frequency changes of the representative panel. To adjust the PPF filter parameters an open-loop adaptation method and an auto-tuning method are investigated. The open-loop adaptation method uses a measurement of the plate temperature and a look-up table with pre-determined parameters to update the filters accordingly. The auto-tuning methods identifies the frequencies of the poles and zeros in the structure's collocated transfer function. From the knowledge of the pole and zero locations the optimal PPF parameters are calculated online.

The results show that both adaptation methods are capable of reducing the vibration levels of the test specimen over the temperature range of interest. Three PPF filters with parameter adaptation through temperature measurement achieve magnitude reductions of the resonance peaks as high as 13.6 decibel. Using the auto-tuning method resonance peak reductions up to 17.4 decibel are possible. The pole/zero identification routine proves to detect the frequencies correctly. The average identification error remained at around one percent even in the presence of external disturbances.

Acknowledgements

I am deeply indebted to many people who helped me pursuing and finishing this research. First of all, I would like to thank Dr. Daniel Inman for serving as my advisor. His guidance and support during my time here at Virginia Tech was always greatly appreciated. I am especially grateful that he gave me the opportunity to work on the Raytheon project. I would also like to thank Dr. Mehdi Ahmadian for serving in my graduate committee and for providing the facilities of the Advanced Vehicle Dynamics Laboratory (AVDL) for the experimental part of this thesis. Special thanks go the third member of my graduate committee, Dr. Donald Leo for being a great teacher and always having the patience to explain a Matlab or controls problem.

Many people from the Center of Intelligent Material Systems and Structures (CIMSS) contributed to this work. I would like to thank Andrew DeGuilio for working with me in the lab on the Raytheon project. Very special thanks go to Beth Howell who was always willing to leave her own work to help me solve administrative problems.

I gratefully acknowledge the support of my graduate studies by Raytheon Systems Company, the Airforce Office of Scientific Research (AFOSR) Grant Number F4962-99-1-0237, and the National Science Foundation (NSF) Grant Number CMS-9713453-001. Without their support this research may have never been done.

I would also like to thank my family and all my friends. Their support and friendship made my time at Virginia Tech enjoyable. Finally and foremost, I would like to thank Janice Matheson for always being there. All her love and understanding helped me through the most difficult hours of this work.

Contents

List of Tables and Figures

Chapter 1

Introduction

This chapter presents an introduction to the research conducted on a vibration suppression system for flexible structures subject to thermal changes. In the first part, the motivation for this study is given followed by information about other studies performed on the same test article. The objectives for this research are summarized in Section 1.2. The third section reviews some of the published literature particularly on positive position feedback and active structural control. The chapter ends with a description of the outline of this thesis.

1.1 Motivation

Structural vibration suppression has attracted the attention of engineers since machines with moving parts and vehicles were invented. Especially the reduction of noise caused by structural vibrations and the diminishing of devastating vibrations have been of great interest. Governed by the need of lightweight solutions for the aerospace industry, active vibration control techniques have experienced rapid developments in the last thirty years. While conventional approaches with passive damping materials minimize structural vibrations they add substantial amounts of weight to the structure and are minimized in their performance. However, active control techniques using smart materials offer light weight high performance solutions to vibration problems. Smart material based actuators and sensors are generally small and lightweight and hardly contribute to the total mass of the structure. They are also unobtrusive.

Rising costs for gasoline and increased environmental concerns, have compelled the automotive and aircraft industries to search for lighter damping solutions for their products. The weight penalty in a Boeing 747 is about 1.5 tons (3500 pounds) of passive damping material and between 3.5 and 22.5 kilograms (8 and 50 pounds) in automotive applications. Decreasing the

mass of passive damping materials in today's automobiles could lead to better fuel economy and, hence, lower the emission of greenhouse gases and pollution. Active vibration control systems retain low noise standards, while at the same time reducing the mass of passive damping materials. Containing more than one ton of passive vibration damping materials modern commercial airplanes are another example with a high potential for benefiting from reduced weight and decreased vibration and noise levels. Assuming a constant lift-off weight for an airplane, active vibration control can help to transport more cargo in one flight and, therefore, reduce the number of necessary fights.

Both industries, the automotive and the aircraft are spending millions of Dollars every year on research for new lighter materials and new technologies like active vibration damping. A recent research project of the Advanced Vehicle Dynamics Laboratory (AVDL) at Virginia Tech was made possible by an automotive supplier. The project included the design of a vibration test rig for flat plates representing an automotive or aircraft structure. Running vibration and noise level tests the feasibility of shunted piezoelectric ceramic patches (PZTs) was analyzed. Another study, sponsored by an aircraft company and conducted by the Center of Intelligent Material Systems and Structures (CIMSS) at Virginia Tech, used optical strain sensors, PZT actuators, and an active vibration control system. The comparison to the passively shunted PZTs showed clear advantages of the active control technique but also staked out the limits of the used active positive position feedback (PPF) controller. Figure 1.1 presents a picture of the developed vibration test stand with electromagnetic shaker and excitation frame in operating position.

Figure 1.1. Vibration Test Stand with Electromagnetic Shaker and Excitation Frame.

During a flight, aircraft structures are exposed to a wide range of temperatures. To test if the actuators and sensors work properly under those changing conditions the temperatures of the test plate were increased from room temperature up to 65°C (150°F). PZT actuators and sensors appeared to function correctly, however, the properties of the test specimen changed significantly with rising temperature. The first vibration mode, for instance, shifted from about 50 Hz at room temperature to over 100 Hz at 65°C (150°F). A short discussion of this phenomenon can be found in Section 4.3. The consequence was that PPF controllers tuned to damp out vibration at room temperature were not effective at increased plate temperatures. Therefore, vibration control of aircraft structures will require an adaptation algorithm to adjust the active controller for the changing structure properties.

1.2 Research Objectives

The objectives for this research can be summarized as:

- select an actuator/sensor system suitable for active control over the temperature range of interest,
- increase the structural damping of the first three to four vibration resonance modes over this temperature range using positive position feedback (PPF) filters,
- develop an algorithm to tune the PPF filter parameters automatically,
- analyze the performance of the closed loop system under undisturbed conditions and under the presence of external disturbances.

1.3 Literature Review

Structural vibration control has experienced rapid development in the last thirty years. Mostly driven from space applications, many new active control techniques have been developed. One of the useful techniques is positive position feedback (PPF) control. Since PPF was first introduced by Caughey and Goh in 1982 several researchers have employed and modified the technique in their own studies. Caughey and Goh also published a study comparing collocated velocity feedback to PPF (1985). They derived the nondynamic stability criterion and showed that PPF stability is not dependent on knowing the internal damping parameters of a structure. PPF controller are basically a special form of second order compensators.

Fanson and Caughey (1990) developed the method further and showed that PPF was capable of controlling the first six bending modes of a cantilever beam. The second order PPF filter was simple to implement and had global stability conditions, which were easy to fulfil even in the presence of actuator dynamics. Integrating new technologies, Fanson and Caughey also used piezoceramics as sensors and actuators.

Goh and Lee (1991) realized that effective vibration control with PPF depends on the accuracy of the modal parameters used in the control design. They extended the original feedback technique with an adaptive estimation procedure to identify the structural parameters.

Using a third-order Butterworth filter, and assuming that the plant parameters lie within bounds of ±20% of their actual value, the adaptive controller achieved good vibration suppression results on a scalar second-order plant. However, for the multi-mode case and persistent excitation, it is shown that simultaneous parameter estimation and control may possibly lead to erroneous results. Goh and Lee illustrated the ineffectiveness of the closed loop adaptive estimation in experiments and suggested open loop estimation with a known probing signal.

Baz et al. introduced a first order PPF filter in 1992 eliminating one of the three filter parameters. They also combined the positive position feedback with independent modal space control. Together with Poh, Baz (1996) presented the effectiveness of the optimal modal positive position feedback algorithm in damping out two vibration modes of a cantilever beam with one piezoelectric actuator and three position sensors. Using a model reference approach, Baz and Hong (1997) illustrated that an adaptive first order PPF filter can successful damp vibration of a cantilever beam even if the first mode changes by 20%.

Another technique to adaptively tune the PPF filter parameters in real time was suggested by Kwak and Han (1998). Kwak and Han utilized a genetic algorithm (GA) to adapt the filter frequency of a single second order filter in a simulation. Filter damping ratio and the gain were kept constant. Later studies [Kwak, Shin, 1999; Kwak, Denoyer, 1999] presented experimental results using GA-tuned PPF filters for vibration suppression. The authors state that the automatic real time tuning of the filter frequencies gave much better results than fixed parameter filters. To employ the adaptive technique the PPF filter was implemented in a digital signal processor (DSP) board, while the genetic algorithm ran on a PC with access to the DSP memory to update the PPF parameters.

Digital PPF filters were first investigated in Fagan's extensive work in 1993. Fagan proposed a root locus design technique in the digital domain for tuning digital PPF filters. He also addressed stability issues of the digital systems and analyzed effects of different sampling rates for the filters. The Tustin transformation was found to map the filter transfer functions correctly into the discrete time domain.

A completely new sensor concept was introduced by Dosch et al. (1992, 1993, and 1995) with the self-sensing actuator. Dosch's studies employed a single piece of piezoceramic material to simultaneously sense and actuate in a closed loop system. The method included a bridge

circuit to separate the actuation signal from the sensing signal. The study also indicates a controller with two PPF filters as the most effective among the analyzed controllers.

Several other damping techniques for structures have been under investigation. For instance, Forward suggested passive shunting of piezoelectric materials (PZT) in 1979. Other authors developed the technique further and published experimental results [Hagood, Flotow, 1991; Aldrich et al., 1993; Jeric, 1999]. In 2000, DeGuilio conducted a research comparing the passive shunting technique to active control with up to six PPF filters. He states that the active control was more effective in reducing vibration levels of a plate than passive shunting. Furthermore, he remarks that passive shunting required three PZT actuators on the structure while the active PPF technique achieved the vibration reduction with only one PZT actuator.

As any narrow band active control system, positive position feedback reaches its best results if tuned properly to the characteristics of the structure to be controlled. For every system containing a plant and active controller, there exists one a set of optimal parameters to fulfil the control objectives and restrictions. Goh and Lee (1991) presented design parameters for PPF filter depending on the structural damping ratios and frequencies to achieve the maximum amount of damping. Using a second order plant model and a second-order PPF filter, McEver (1999) states that the optimal parameters can be derived from the ratio of the structural pole frequencies to the structural zeros $\omega_{zp} = \omega_z / \omega_p$. He proposes a very simple algorithm for obtaining the three PPF filter parameters damping, frequency, and gain. An online zero/pole identification method was also developed. In this way, McEver was able to automate the tuning process of one second-order PPF filter.

1.4 Outline of Thesis

This thesis is structured in seven chapters. Chapter 1 gives an introduction to the material and reviews literature published on similar studies. In Chapter 2, some background information is provided. The chapter addresses fundamentals of piezoelectric materials and an overview over adaptive control techniques.

The positive position feedback (PPF) theory is presented in the third chapter. The section reviews the conventional PPF technique and shows the derivation of the optimal PPF parameters depending on the ratio of the zero and pole frequencies of the structure. Furthermore, aspects of digital PPF filters are addressed in this part of the thesis.

The experimental section of this research begins with Chapter 4. The mechanical test stand design is described as well as the actuator and sensor placement on the test plate. The forth chapter also informs about the signal conditioning hardware and the data acquisition system used. Finally, at the end of this chapter, the performed baseline tests are summarized and a decision for the accelerometer as a sensor is made.

Chapter 5 starts with the description of the algorithm to change the PPF filter parameters according to the measured temperature. The use of a thermistor is described and its connection to the digital signal processor (DSP) board. Test results with the temperature measurement algorithm are represented in the second part of Chapter 5. The results illustrate that for known temperature behavior of structures a temperature sensor can be an alternative to more complicated self-adapting controllers.

For uncertain temperature dependencies of the structure, an online pole/zero identification algorithm is examined in Chapter 6. As the results show, the algorithm is able to identify the pole and zero frequencies correctly even in the presence of noise. With the obtained information about the structure, PPF filters can be tuned automatically.

Finally, the results of this research are summarized in the conclusions, Chapter 7. This last chapter also discusses possibilities for future work.

Chapter 2

Background

This chapter provides some background information on the piezoelectric effect and how it can be used as smart material in actuators and sensors. In the second part a brief overview of adaptive control techniques is given.

2.1 Piezoelectric Theory

Piezoelectricity is a phenomenon observed in certain crystals, e.g., quartz and Rochelle salt, ceramic materials, and even polymers. Piezoelectric materials that are exposed to mechanical stress (pressure) generate an electric voltage between material surfaces. This is known as the direct piezoelectric effect. Conversely, if the materials are subject to an electric field the crystals show mechanical deformation (converse piezoelectric effect). This coupling between electrical and mechanical energy makes the materials very useful as transducers in many applications. Typical applications include microphones, ultrasonic transmitters, phonograph cartridges, electrical oscillators in high frequency circuits, and many more. This research employs piezoelectric materials as strain gauges and strain generators.

Piezoelectricity occurs only in crystals without a center of symmetry in the smallest unit of the crystal. By applying mechanical pressure to the material, the ions of those unit cells become displaced causing an electrical polarization of the cell. Finally, the polarization effects add up within the crystal generating the electric voltage on the surfaces. The converse piezoelectric effect happens in a similar way. The external electrical field induces an electrostatic force on the ions leading to small displacements of the ions in the unit cell. The displacements of the ions, furthermore, cause the deformation of the whole crystal.

Because the piezoelectric effect is not very strong in quartz and other natural crystals, piezoelectric polycrystalline ceramics such as Barium Titanate ($BaTiO_3$) and Lead Zirconate Titanate ($Pb(ZrTi)O_3$) were developed. Lead Zirconate Titanate based ceramics, also known as PZTs, are the most common piezoelectric ceramics in modern sensor and actuator applications. In contrast to piezoelectric crystals where piezoelectricity occurs naturally, the piezoelectric properties of the polycrystalline ceramics have to be induced by a process called poling. The raw material contains randomly oriented groups of electric dipoles called Weiss domains. Poling aligns the Weiss domains in the material by applying a very strong electric field to the heated ceramic. After the poling process, all electric dipoles within the material are arranged in parallel and the material shows piezoelectric characteristics.

Due to the polarization and the anisotropic structure of the material, piezoelectric properties depend on the relative direction to the poling axis. To distinguish between the different coefficients engineers have developed a system of subscripts and superscripts for the material coefficients to identify the directions and measurement conditions. For commonly accepted definitions see [Physik Instrumente (1), 1999] or [SensorTech, 1999]. The piezoelectric coefficients and other material constants for the PZTs used in this research are listed in Appendix E. Due to the fact that the PZTs used in this research have a square shape, the open-loop actuation equations become relatively simple. The static displacement in the transverse direction without any force applied can be calculated as

$$\Delta w = \frac{d_{31} V w}{t} \tag{2.1}$$

where V is the applied voltage, w is the width and length of the PZT, t is the thickness of the PZT, and d_{31} is the piezoelectric charge coefficient in 3-1-direction. The numbers represent the axes in a 3-D Cartesian coordinate system whereas the 3-axis conforms to the poling direction. The static displacement in the thickness of the material can be calculated as

$$\Delta t = d_{33} V \tag{2.2}$$

where d_{33} is the piezoelectric charge coefficient in 3-3-direction. Note that the equations are valid only if the actuator can move freely, i.e. the actuator does not generate any force (open-loop). Bonding PZTs to a flat structure such as a steel plate in this research transforms the

transverse displacement into a distributed bending moment applied from the actuator to the structure.

Because there exists a counterpart to the piezoelectric effect, the converse piezoelectric effect, the same material can also be used as a sensor. The open-loop (no current is drawn) sensor equations for a square PZT sheet can be formulated as

$$V = \frac{g_{31} F_1}{w} \tag{2.3}$$

where V is the output voltage, g_{31} is the piezoelectric voltage coefficient in 3-1-direction, and F_1 is the applied transversal force. The voltage for an applied perpendicular force (F_3) can be calculated as

$$V = \frac{g_{33} F_3 t}{w^2} \tag{2.4}$$

where g_{33} is the piezoelectric voltage coefficient in 3-3-direction. For a sensor bonded to the surface of a plate, Equation 2.3 applies. Due to the mechanical coupling to the structure, the sensor generates a voltage proportional to the mechanical strain distribution at the sensor location.

Besides square shaped PZT sheets, many other forms of PZTs are possible. Most manufactures of piezoelectric ceramics offer a wide variety in shapes and forms to cover different applications. [Physik Instrumente (2), 1999; Piezo Systems (1)]. One of the well-developed applications is the use of piezoelectric materials in accelerometers. Depending on the requirements for the output signal, crystalline quartzes or polycrystalline piezoelectric ceramics are utilized. The accelerometers used in this research contain ceramics as active transducers.

To transform the mechanical energy into an electrical signal a variety of mechanical configurations are available. Older accelerometer configurations utilized the compression design where a seismic mass compresses and stretches the piezoelectric material. Modern configurations contain either the shear mode design or the flexural mode design. Flexural mode design uses beam-shaped sensing crystals, which are supported only in the middle. Acceleration causes the free ends to bend up or down, hence, mechanical strain is induced and voltage is generated. The accelerometers used in this research utilize the shear mode design where the piezoelectric material is bonded between a center post and a ring-shaped seismic mass. Under

acceleration, the seismic mass induces shear stress in the transducer material generating a voltage, which is proportional to the occurring acceleration. Figure 2.1 shows the design principle of a shear mode accelerometer in profile. The arrows indicate the motion due to acceleration in upward direction. The shear mode design is most widely used in modern accelerometers as it offers a large frequency range, low off-axis sensitivity, low sensitivity to base strain and low sensitivity to temperature variations.

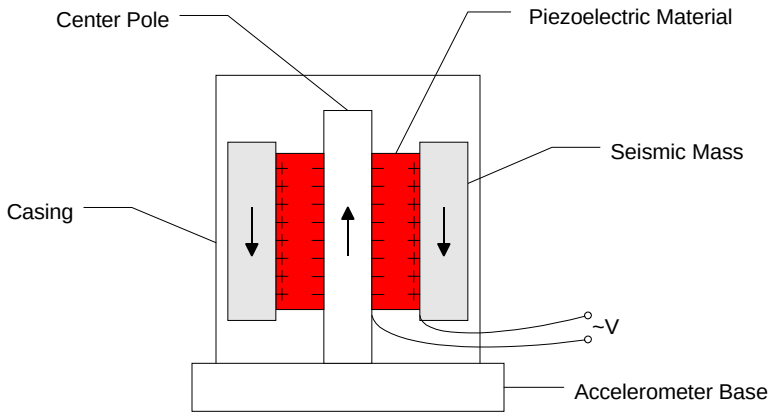

Figure 2.1. Design Principle of a Shear Mode Accelerometer.

This section has offered an introduction to the piezoelectric effect and its applications in sensors and actuators. Since this research utilized square-shaped PZTs as actuators, the simplest actuator equations for this case were presented. The section also gave a short overview of the use of piezoelectric materials in accelerometers. The next section introduces in the wide field of adaptive control.

2.2 Adaptive Control Overview

Adaptive control has been under intense investigation in the last fifty years. Early developments were driven from the need of autopilots for high-performance airplanes [Åström, 1989]. Researchers found that conventional static-gain feedback controllers could not work well over the wide range of speeds and altitudes. In the 1960s, adaptive control techniques experienced a

revolution with the introduction of the state space and stability theory. Today, many commercial solutions are on the market implementing adaptive techniques with digital microcontrollers.

Many attempts have been made over the years to define the term “adaptive control.” Although a standard definition does not seem to exist in the literature, there exists a set of common concepts. These concepts suggest that an adaptive system should include parameter adjustments to counter variations in the dynamics of the process or of the plant. In most cases, the achieved behavior is compared to the desired behavior to obtain a measurement of the performance. Therefore, adaptive control offers a solution for significant variations in the process dynamics and for variations in the disturbances. Due to the parameter adjustments within the controller, adaptive systems are highly non-linear. This can make the analysis for global stability of the system very complicated.

Several adaptive schemes have been developed since research on adaptive systems began in the 1950s. Those schemes include model reference adaptive control (MRAC), self-tuning regulators (STR), and gain scheduling. Model reference control utilizes an “ideal” model of the plant. The adjustment mechanism varies the controller parameters until the behavior of the plant/controller system matches the behavior of the reference model. Figure 2.2 shows the block diagram of a MRAC system. Notice that the system contains two loops. There is an inner loop, which is the conventional feedback loop, and there is an outer loop containing reference model and the parameter adjustment mechanism.

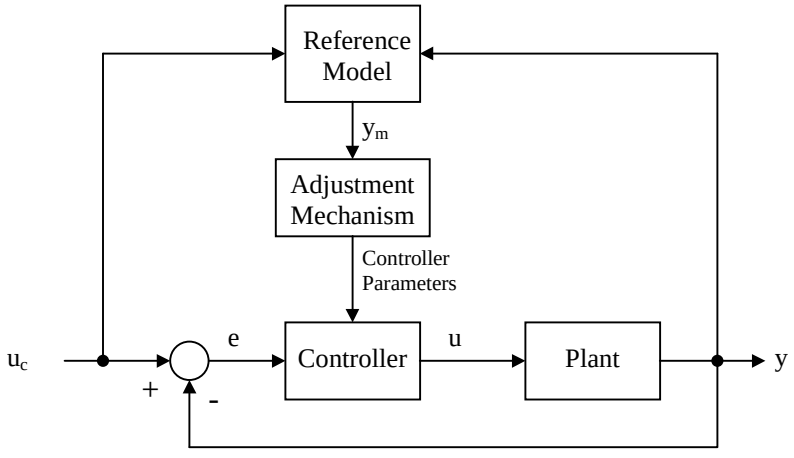

Figure 2.2. Block Diagram of a Model Reference Adaptive Control System.

The second, very important adaptive control scheme is the self-tuning regulator. Similar to the model reference approach, self-tuning regulators contain an inner and an outer feedback loop. In contrast to MRAC where the system behavior is matched to a reference, STR attempts to identify the plant. The plant parameters are estimated using the input and the output of the plant. Using those plant parameters, an on-line design procedure calculates the controller parameters. Figure 2.3 represents the block diagram of a self-tuning regulator. The STR scheme is very flexible with respect to the choice of the underlying controller design procedure and the estimation methods, therefore many different combinations can be used [Åström, 1989].

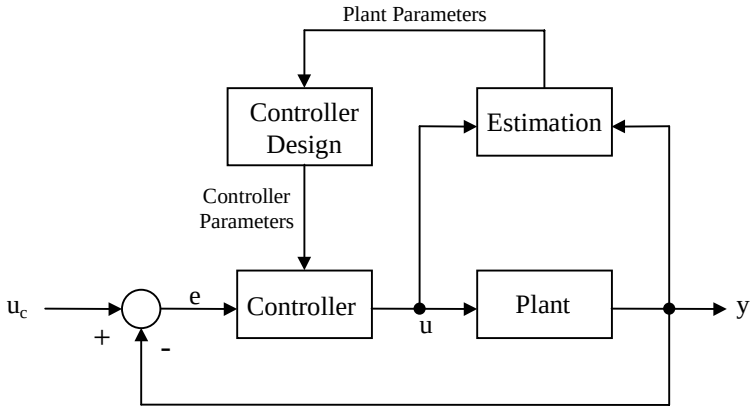

Figure 2.3. Block Diagram of a Self-Tuning Regulator System.

Neither of the two adaptive schemes was actually used in this research. MRAC did not seem well suited for the problem. Having a reference model for the test plate with highly damped vibration modes could lead to decent performance of the active control system. However, the significant shifts of the test plate's mode frequencies due to temperature variations would require either a new reference model for each temperature or a vast control effort (actuator voltage) to drive the mode frequencies back to the original frequency values. The STR could not be implemented in its original form due to the lack of a suitable on-line estimation method for the multi-order plant.

Instead of using those closed-loop adaptation schemes, an open-loop scheme called gain scheduling was investigated first. Gain scheduling measures external operating conditions which lead to the variations in the plant parameters. This measurement is used to update the controller parameters from the schedule. The schedule has to be determined beforehand, experimentally, or analytically. As it can be seen in Figure 2.4, gain scheduling is an open-loop adaptation method, meaning there exists no feedback path from the output of the plant to the controller parameter computation. With regard to some definitions of adaptive control, gain scheduling is not always considered an adaptive technique. The gain scheduling controller used in this research for vibration suppression is described in Chapter 5. The operating condition measured was the temperature of the test structure.

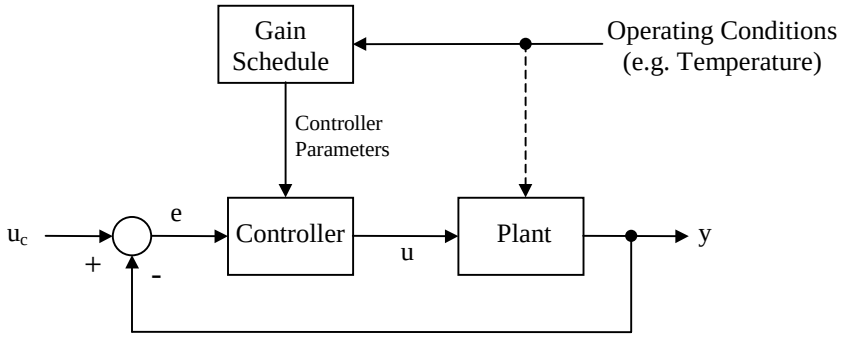

Figure 2.4. Block Diagram of a System with Gain Scheduling.

Because there exists no feedback to the controller parameter computation, the gain scheduling might follow an incorrect schedule. To overcome this disadvantage of the open-loop process, another adaptive scheme called auto-tuning was investigated in this research. Auto-tuning represents a modified STR system where the plant identification and the controller design are initiated by an operator. After the controller parameters are calculated, the system switches in the "control mode" and no further parameter adjustments are done. Figure 2.5 shows the elements of a system with auto-tuning. Note that the system contains a block labeled "Probe Signal." The probe signal is used to excite the plant in a defined way, hence simplifying the estimation process. Although many different excitation signals such as random excitation, fixed

sine excitation, or impact excitation are possible as probe signals this research utilized a sine sweep signal as probe the signal. The description of the auto-tuning controller used in this research can be found in Chapter 6. Due to the lack of continuous parameter adjustments, auto-tuning is not considered as an adaptive control technique by many definitions of adaptive control.

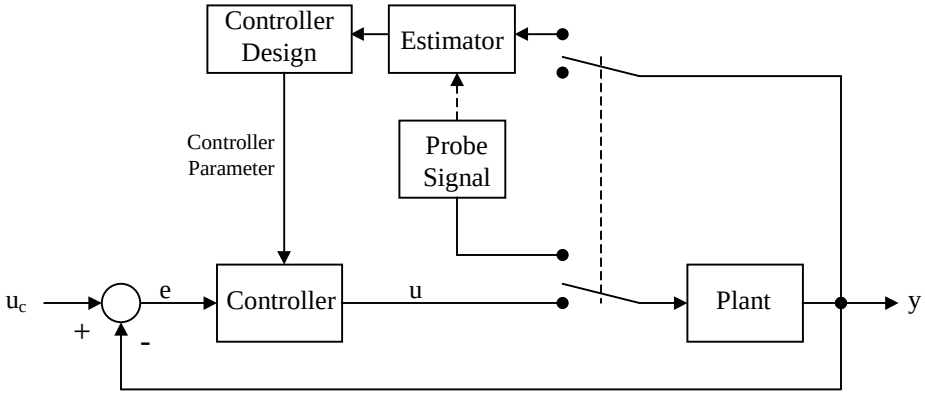

Figure 2.5. Block Diagram of a System with Auto-Tuning.

This section has presented an overview over the most common adaptive control techniques. Adaptive control was introduced as a technique to counter variations in the dynamics of the plant. Pure adaptive techniques such as model reference adaptive control and self-tuning regulators were presented as well as semi-adaptive techniques, such as gain scheduling and auto-tuning. The gain scheduling method and the auto-tuning method will be used in Chapter 5 and Chapter 6 to implement positive position feedback filters for vibration suppression over a wide temperature range. The next chapter will introduce in the positive position feedback technique.

Chapter 3

Positive Position Feedback

This chapter provides an overview of the positive position feedback (PPF) technique. In the first section general information about PPF is given. The second section shows the derivation of the optimal filter parameters. This derivation itself is not original and can also be found in [McEver, 1999]. Finally, Section 3.3 introduces the digital PPF filter. Aspects of transformation and sampling rate are presented.

3.1 PPF for Structural Control

The technique of positive position feedback (PPF) control was first introduced by Caughey and Goh in a Dynamics Laboratory Report in 1982. Its simplicity and robustness has led to many applications in structural vibration control [Agnes, 1997; DeGuilio, 2000; Dosch, 1992 and 1993; Fanson et al., 1990; Leo, 1994; McEver, 1999; Scruggs, 1999]. Unlike other control laws, positive position feedback is insensitive to the rather uncertain natural damping ratios of the structure [Goh and Caughey, 1985]. The terminology positive position is derived from the fact that the position measurement is positively fed into the compensator and the position signal from the compensator is positively fed back to the structure [Fanson and Caughey, 1990]. This property makes the PPF controller very suitable for collocated actuator/sensor pairs. Equations 3.1 and 3.2 show the structure and compensator equations in the scalar case:

Structure: $$\ddot{\xi} + 2\zeta\omega\dot{\xi} + \omega^2\xi = g\omega_f{}^2\eta \tag{3.1}$$

Compensator: $$\ddot{\eta} + 2\zeta_f\omega_f\dot{\eta} + \omega_f{}^2\eta = \omega^2\xi \tag{3.2}$$

where g is the scalar gain (positive), ξ is the modal coordinate (structural), η is the filter coordinate (electrical), ω and ω_f are the structural and filter frequencies, respectively, and ζ and ζ_f are the structural and filter damping ratios, respectively. A Nyquist stability analysis of this system leads to the necessary and sufficient condition for stability: 0 < g < 1 [Fanson and Caughey, 1990]. This non-dynamic stability criterion is characteristic for the positive position feedback system. Figure 3.1 illustrates the connection of Equations (3.1) and (3.2) in a block diagram.

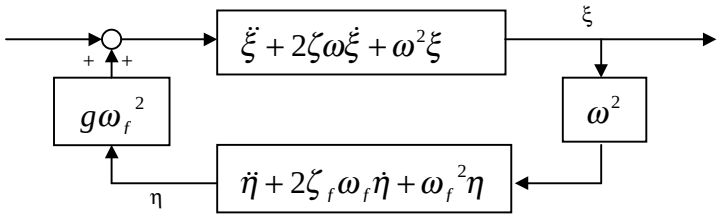

Figure 3.1. Block Diagram of a Second-Order System with Positive Position Feedback.

The second-order transfer function in Equation 3.3 also represents the PPF compensator. The transfer function form will be used in this text for deriving the properties of the control system.

$$G_{PPF}(s) = \frac{g\omega_f{}^2}{s^2 + 2\zeta_f\omega_f s + \omega_f{}^2} \tag{3.3}$$

Another feature of the compensator equation, its second-order low-pass characteristic, led to the terminology PPF filter. Figure 3.2 presents a Bode plot of a typical PPF filter. In effect, a PPF filter behaves much like an electronic vibration absorber for the structure except that a mechanical vibration absorber can never destabilize a structure.

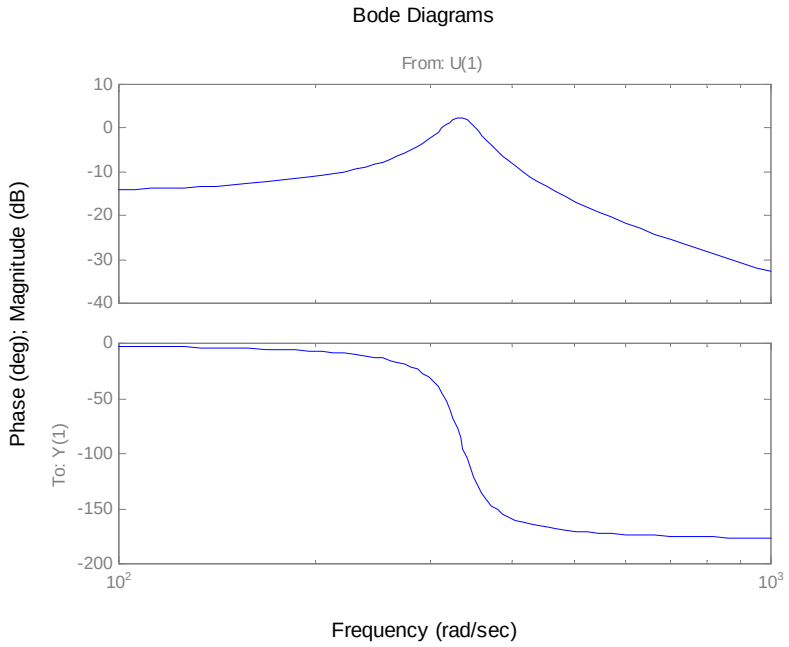

Figure 3.2. Bode Plot of a Typical PPF Filter Frequency Response Function.

The roll-off character of the PPF filter is one of the advantages of using a PPF controller. Structural poles with frequencies higher than the filter frequencies are hardly affected by the compensator. This is especially useful when complicated structures with many resonance poles are to be controlled. PPF is able to add damping to lower frequency poles while leaving the possibly unmodeled high frequency poles unchanged.

Since one PPF filter tuned to a certain frequency only adds damping to one certain pole of the structure the possibilities of multiple PPF were investigated by many authors [DeGuilio, 2000; Goh and Caughey, 1985; Fanson and Caughey, 1990]. Multiple PPF filters allow that each filter is tuned to add damping to one structural pole while only using one actuator/sensor pair. As an example, three PPF filters are used in the block diagram in Figure 3.3. Unfortunately, the stability criterion is not as simple as for the one PPF filter case but experiments have shown that for widely spaced poles with up to three PPF filters the stability is usually not a problem [DeGuilio, 2000]. Fanson and Caughey published a multivariable stability criterion for the general collocated control implementation of PPF in 1990.

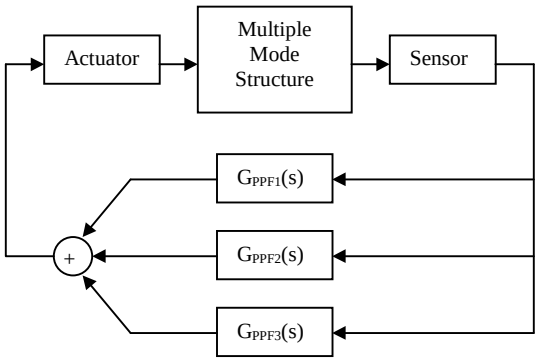

Figure 3.3. Three PPF Filter Implementation with One Collocated Sensor/Actuator Pair on the Structure.

3.2 Optimal PPF Parameters

The simplicity and easy to maintain stability criterion of the PPF controller made the PPF control law the first choice as an active vibration controller for the representative aircraft panel. Although the transfer function $G_{PPF}(s)$ only contains three parameters, they still had to be determined. The three parameters are the gain g, the filter damping ratio ζ_f, and the filter frequency ω_f. To determine the values of the parameters the principle of tuning was introduced in the literature. Most authors suggest a value for the filter frequency ω_f slightly greater than the structural frequency to be damped. While Dosch, Inman, and Garcia (1992) specified a factor of 1.3 between ω and ω_f, Fagan (1993) chooses 1.45. The range for the filter damping ratio found in the literature reaches from $\zeta_f = 0.01$ to 0.5. In many experiments described in the literature the authors would find a compromise value for ζ_f, and leave it constant through all their experiments. Some authors [Fagan, 1993; Goh and Caughey, 1985] use a certain pole placement technique to compute the three parameters. That ensures minimal gains at a maximum closed loop damping ratio. However, an exact model of the poles of the structure to be damped is required. Other authors [DeGuilio, 2000; Dosch, Leo, and Garcia 1992; Fanson and Chen, 1986] only used information about the frequency of the pole to be damped and determine the parameters with a trial and error technique experimentally.

McEver (1999) was the first one presenting a method to compute all three parameters of the PPF filter from information about the pole/zero pair in the transfer function of the structure. The derivation of this method is shown in the following paragraphs. Although the derivation is not original, it is essential for understanding the experiments later in this work. The development of the equations can also be found in [McEver, 1999].

For the analysis, a typical collocated control-to-output frequency response of a structure is assumed. The response function is characterized by a number of alternating poles and zeros. Figure 3.4 shows an example of such a function with four vibration modes. To simplify the analysis only one pole/zero pair of the transfer function will be considered. This also conforms to the second-order system in Equations (3.1). The bode plot of the simplified system is shown in Figure 3.5.

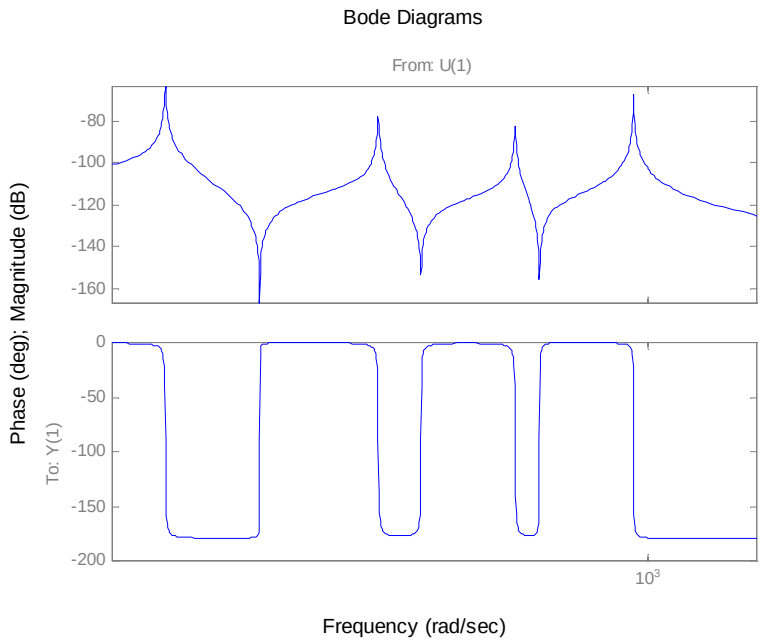

Figure 3.4. Bode Diagrams of a Typical Collocated Control-to-Output Frequency Response of a Structure.

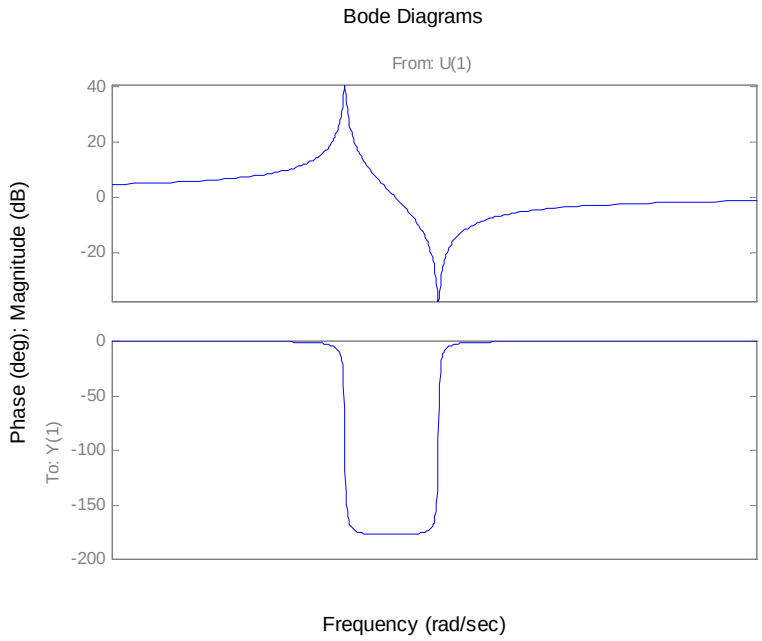

Figure 3.5. Bode Diagrams of a Collocated Control-to-Output Frequency Response for a Second-Order System.

The objective now is to increase the damping of the pole of the system shown in Figure 3.5. Closing the feedback loop, as shown in Figure 3.6, results in a closed loop system with four poles and two zeros. Figure 3.7 presents a root locus plot of the resulting closed loop system where small crosses indicate the location of the poles and small circles indicate the location of the zeros on the complex plane. As the PPF filter gain g is increased, the structural poles move from their original location close to the imaginary axis further into the left half plane. Notice that at the same time the filter pole moves towards the structural zero, decreasing its damping ratio.

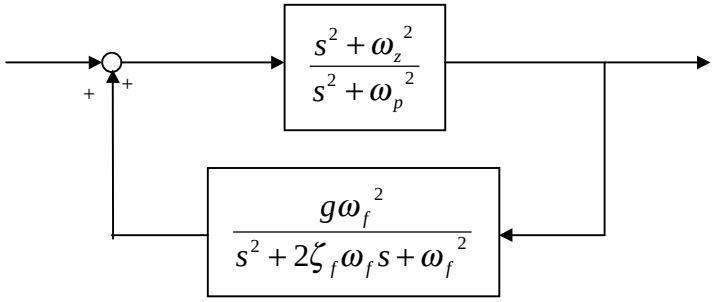

Figure 3.6. Block Diagram of Second-Order Plant and PPF Filter in the Feedback Path.

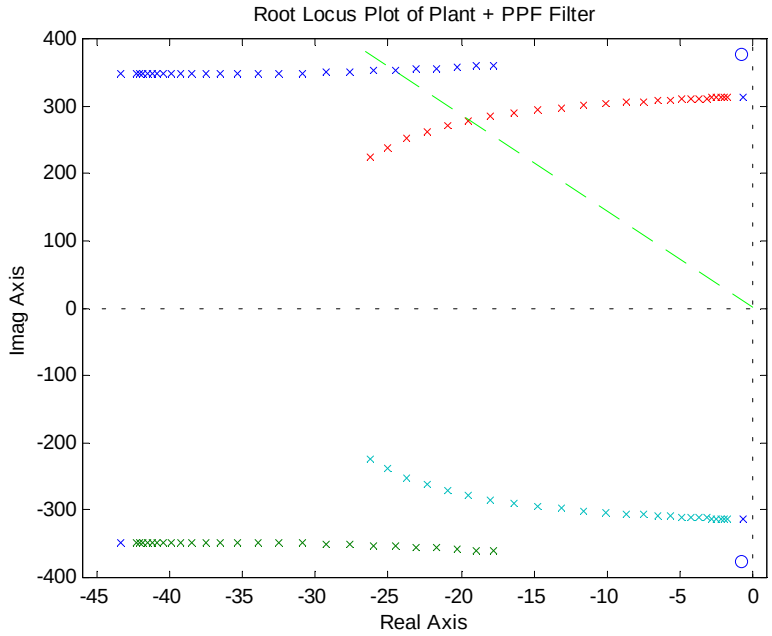

Figure 3.7. Root Locus Plot of the Second-Order System and the PPF Filter in the Feedback Path.

To maximize the damping in the closed loop system while using the minimal value for the compensator gain a set of optimal closed loop pole locations is desired. These optimal locations turn out to be where all resulting closed loop poles have an equal damping ratio. In other words, the filter pole and the structural pole lay on one line emanating from the origin. The dashed line in Figure 3.7 represents such a line of equal damping. Figure 3.8 demonstrates the geometrical relationship between the pole locations and the closed loop parameters in the second

quadrant. Using the law of similar triangles the frequency of the second pole can be expressed as a multiple α of the frequency of the first pole or

$$\omega_2 = \alpha\omega_1 . \tag{3.4}$$

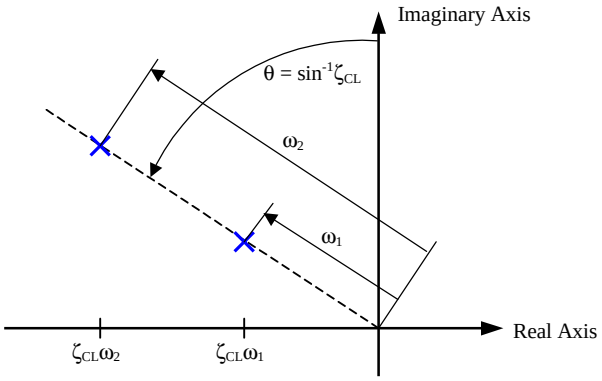

Figure 3.8. Geometrical Relations of the Optimal Closed Loop Poles.

From the knowledge of the optimal closed loop pole locations the optimal parameters of the positive position feedback filter g, ζ_f, and ω_f can be derived. The simplest case of a second-order system, a transfer function with one pair of undamped complex poles and one pair of complex zeros, was considered for the structural plant:

$$G_y(s) = \frac{s^2 + \omega_z{}^2}{s^2 + \omega_p{}^2} \tag{3.5}$$

where ω_p is the frequency of the pole and ω_z is the frequency of the zero both in radians per second. As shown later the optimal parameters depend on the ratio of those frequencies so the zero-pole spacing ω_{zp} is defined as $\omega_{zp} = \omega_z / \omega_p$. It is also helpful to transform the Equations (3.3) and (3.5) into transfer functions of the non-dimensional frequency σ by using $s = j\omega_p\sigma$:

$$G_{PPF}(\sigma) = \frac{-g\omega_{fp}{}^2}{\sigma^2 - 2j\zeta_f\omega_{fp}\sigma - \omega_{fp}{}^2} \tag{3.6}$$

$$G_y(\sigma) = \frac{\omega_{zp}{}^2 - \sigma^2}{1 - \sigma^2} \tag{3.7}$$

where j is the imaginary unit and ω_{fp} is the normalized filter frequency $\omega_{fp} = \omega_f / \omega_p$. Using Equations (3.6), (3.7), and Figure 3.6, the closed loop transfer function comes out as

$$\begin{aligned} G_{CL}(\sigma) &= \frac{G_{PPF}(\sigma)}{1 - G_y(\sigma) G_{PPF}(\sigma)} \\ &= \frac{(-\sigma^2 + 2j\zeta_f \omega_{fp}\sigma + {\omega_{fp}}^2)({\omega_{zp}}^2 - \sigma^2)}{\sigma^4 - 2j\zeta_f \omega_{fp}\sigma^3 + (-{\omega_{fp}}^2 + g{\omega_{fp}}^2 - 1)\sigma^2 + 2j\zeta_f \omega_{fp}\sigma + {\omega_{fp}}^2 - g{\omega_{fp}}^2{\omega_{zp}}^2} \end{aligned} \tag{3.8}$$

with the characteristic equation

$$\phi(\sigma) = \sigma^4 - 2j\zeta_f \omega_{fp}\sigma^3 + (-{\omega_{fp}}^2 + g{\omega_{fp}}^2 - 1)\sigma^2 + 2j\zeta_f \omega_{fp}\sigma + {\omega_{fp}}^2 - g{\omega_{fp}}^2{\omega_{zp}}^2 \tag{3.9}$$

Considering Equation (3.4) and Figure 3.8 the wanted characteristic equation for the optimal closed loop system can be formed:

$$\phi_{wanted}(s) = (s^2 + 2\zeta_{CL}\omega_1 s + {\omega_1}^2)(s^2 + 2\zeta_{CL}\alpha\omega_1 s + \alpha^2{\omega_1}^2) \tag{3.10}$$

To transform Equation (3.10) into an equation of the non-dimensional frequency σ the relation $s = j\omega_p\sigma$ is used again. Collecting the terms in σ yields to:

$$\begin{aligned} \phi_{wanted}(\sigma) = \sigma^4 &- 2j\zeta_{CL}(1+\alpha)\left(\frac{\omega_1}{\omega_p}\right)\sigma^3 - (\alpha^2 + 4{\zeta_{CL}}^2\alpha + 1)\left(\frac{\omega_1}{\omega_p}\right)^2\sigma^2 + \\ &+ 2j\zeta_{CL}(\alpha + \alpha^2)\left(\frac{\omega_1}{\omega_p}\right)^3\sigma + \alpha^2\left(\frac{\omega_1}{\omega_p}\right)^4 \end{aligned} \tag{3.11}$$

Equating Equations (3.9) and (3.11) and performing a coefficient comparison results in four new equations:

$$\zeta_{CL}(1+\alpha)\left(\frac{\omega_1}{\omega_p}\right) = \zeta_f \omega_{fp} \tag{3.12}$$

$$(\alpha^2 + 4{\zeta_{CL}}^2\alpha + 1)\left(\frac{\omega_1}{\omega_p}\right)^2 = {\omega_{fp}}^2 - g{\omega_{fp}}^2 + 1 \tag{3.13}$$

$$\zeta_{CL}(\alpha + \alpha^2)\left(\frac{\omega_1}{\omega_p}\right)^3 = \zeta_f \omega_{fp} \tag{3.14}$$

$$\alpha^2\left(\frac{\omega_1}{\omega_p}\right)^4 = \omega_{fp}{}^2 - g\omega_{fp}{}^2\omega_{zp}{}^2 \tag{3.15}$$

Notice that Equations (3.12) and (3.14) have the same term on the right side. Therefore, the left sides of both equations have to be equal and α relates to ω_1/ω_p as following:

$$\sqrt{\frac{1}{\alpha}} = \left(\frac{\omega_1}{\omega_p}\right) \tag{3.16}$$

Using that result to substitute ω_1/ω_p in Equations (3.12), (3.13), and (3.15) gives another set of three equations:

$$\zeta_{CL}\left(\sqrt{\frac{1}{\alpha}} + \sqrt{\alpha}\right) = \zeta_f\omega_{fp} \tag{3.17}$$

$$\alpha + 4\zeta_{CL}{}^2 + \frac{1}{\alpha} = \omega_{fp}{}^2 - g\omega_{fp}{}^2 + 1 \tag{3.18}$$

$$1 = \omega_{fp}{}^2 - g\omega_{fp}{}^2\omega_{zp}{}^2 \tag{3.19}$$

Now, given the zero/pole spacing of the structure ω_{zp} and a specific PPF filter gain g Equation (3.19) leads to the normalized PPF filter frequency as a function of g and ω_{zp}:

$$\omega_{fp} = \sqrt{\frac{1}{1 - g\omega_{zp}{}^2}} \tag{3.20}$$

Furthermore, Equation (3.18) can be solved for the closed loop damping ratio:

$$\begin{aligned}\zeta_{CL} &= \frac{1}{2}\sqrt{\omega_{fp}{}^2 - g\omega_{fp}{}^2 + 1 - \alpha - \frac{1}{\alpha}} \\ &= \frac{1}{2}\sqrt{\frac{1-g}{1-g\omega_{zp}{}^2} + 1 - \alpha - \frac{1}{\alpha}}\end{aligned} \tag{3.21}$$

Equation (3.21) clearly indicates that the closed loop damping ratio for certain parameters g and ω_{zp} reaches its maximum at $\alpha = 1$ so that ζ_{CL}, becomes:

$$\zeta_{CL} = \frac{1}{2}\sqrt{\frac{1-g}{1-g\omega_{zp}{}^2} - 1} \tag{3.22}$$

Having the closed loop damping ratio ζ_{CL} enables us to calculate the PPF filter parameter ζ_f. Applying $\alpha = 1$, Equation (3.17) can be solved for the filter damping ratio as a function of the closed loop damping ratio and the normalized filter frequency:

$$\zeta_f = \frac{2\zeta_{CL}}{\omega_{fp}} \tag{3.23}$$

Determining the filter gain g requires a short stability analysis. For positive feedback, instability occurs when the open loop phase is $0° \pm m\,360°$, m = 1, 2, 3, ... [McEver]. This phase angle is reached in the case of a collocated plant transfer function at zero frequency. The open loop transfer function $G_{OL}(s)$ appears to be:

$$G_{OL}(s) = G_{PPF}(s)G_y(s) = \frac{g\omega_f{}^2}{s^2 + 2\zeta_f\omega_f s + \omega_f{}^2}\frac{s^2 + \omega_z{}^2}{s^2 + \omega_p{}^2} \tag{3.24}$$

For zero frequency (s = 0) $G_{OL}(s)$ becomes:

$$G_{OL}(s=0) = \frac{g\omega_f{}^2}{\omega_f{}^2}\frac{\omega_z{}^2}{\omega_p{}^2} = g\omega_{zp}{}^2 \tag{3.25}$$

That means, instability occurs if $g > \frac{1}{\omega_{zp}{}^2}$. Therefore, the gain margin *GM* is defined as:

$$GM = \frac{1}{g\omega_{zp}{}^2} \tag{3.26}$$

The analysis of Equations (3.22) and (3.26) shows that only for a zero/pole spacing greater then one (or $\omega_z > \omega_p$) and a positive gain g Equation (3.22) leads to a real valued solution. The case that the zero/pole spacing becomes less than one ($\omega_z < \omega_p$) is purely theoretical. The collocated transfer function of a real structure will always start with a pole. Hence, the case $\omega_{zp} < 1$ does not need to be considered for practical purposes. Figure 3.9 shows simulations of the closed loop system with optimal and non-optimal PPF parameters compared to the open loop system. Note the significant improvement for the optimal parameters although only the filter damping ratio was altered. The PPF filter frequency and the gain remained the same.

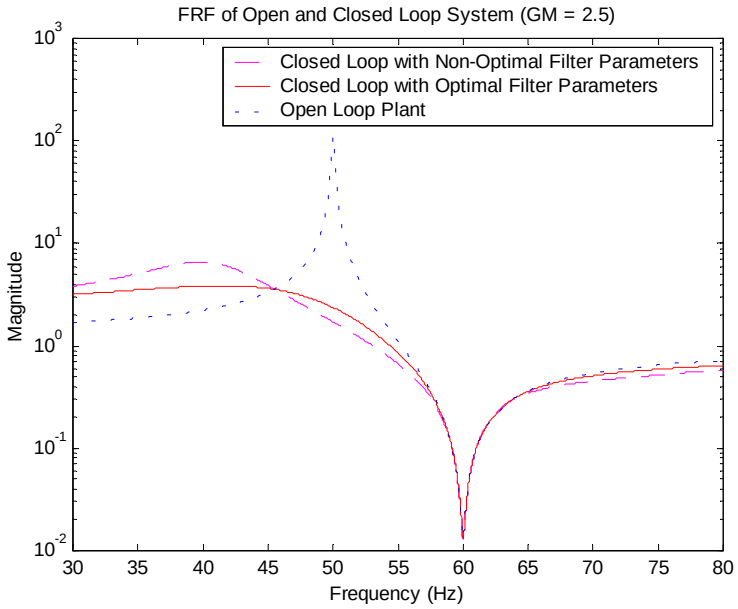

Figure 3.9. Frequency Response Function of Open and Closed Loop System.

An interesting effect can be observed by examining Figure 3.10. The graph shows the ratio of the maximum magnitude of the uncontrolled second-order plant to the maximum magnitude of the controlled plant. The ratio is plotted versus the gain margin *GM* and the zero-pole spacing ω_{zp}. First, the graph supports the statement that a greater spacing of the zero and the pole frequencies results in a higher closed-loop damping ratio. This direct dependency $\zeta_{CL}=f(\omega_{zp})$ was already formulated by [McEver, 1999]. The second observation is that maximum closed-loop damping ratios cannot be achieved with gain margins very close to one. While for small a zero-pole spacing (ω_{zp}.= 1.075) the optimal gain margin lies around 3.5, it decreases to about 2.0 when the zero-pole spacing reaches 1.5. Although the optimal *GM* drops below 2.0 for greater ω_{zp} (>1.75) this is irrelevant for real structures. The zero, following a structural pole in a collocated transfer function of a real structure, remains in the range $\omega_p < \omega_z < 1.5\omega_p$, and therefore, a gain margin should not be chosen smaller than 2.0 for practical purposes. Although not very distinct, experimental results seem to confirm this statement

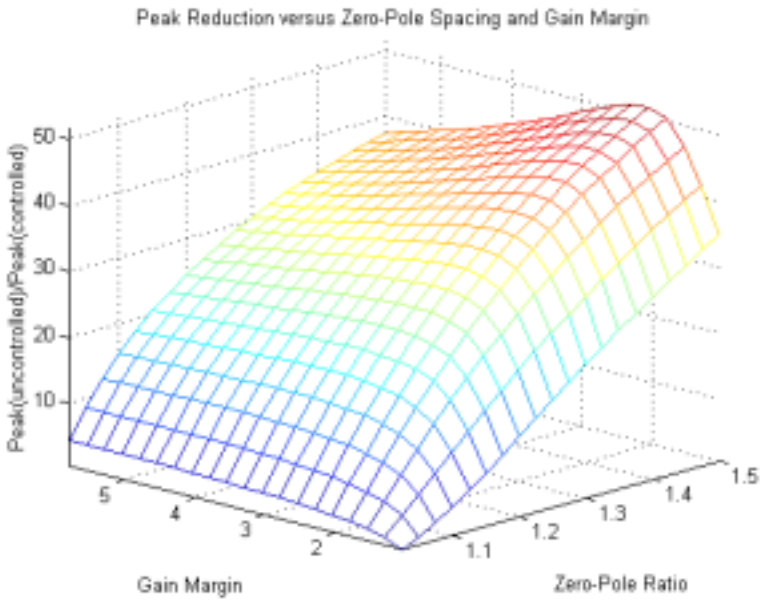

Figure 3.10. Ratio of the Maximum Magnitude of the Open-Loop System to the Maximum Magnitude of the Closed-Loop System versus Gain Margin and Zero-Pole Spacing.

This section has presented the derivation of the optimal parameters of a positive position feedback system. To make a closed form solution possible the simplest case of a collocated transfer function was assumed. Note that most of the presented work is not original and can also be found at [McEver (1999)] but is presented because it is relevant to the work presented here. Summarizing the following algorithm for computing the optimal PPF filter parameters is suggested:

1. Determine the pole and zero frequencies and compute $\omega_{zp} = \omega_z / \omega_p$,
2. Choose a certain gain margin $GM > 1$ suitable for the problem (for practical purposes $GM > 2$),
3. Compute the PPF filter gain: $g = \dfrac{1}{GM\omega_{zp}^{\,2}}$,
4. Calculate the PPF filter frequency with $\omega_{fp} = \sqrt{\dfrac{1}{1 - g\omega_{zp}^{\,2}}}$ and $\omega_f = \omega_p \omega_{fp}$,

5. Determine the closed loop damping ratio $\zeta_{CL} = \frac{1}{2}\sqrt{\frac{1-g}{1-g\omega_{zp}^{\ 2}} - 1}$, and

6. Calculate the PPF filter damping ratio $\zeta_f = \frac{2\zeta_{CL}}{\omega_{fp}}$.

This algorithm will now be used throughout this work to solve for the positive position feedback filter parameters. The PPF design procedures for the experiments in Chapter 5 and 6 will employ the optimal parameter equations to adapt the PPF filters to the changing properties of the plant.

3.3 Digital PPF Filter

The availability of powerful microcontrollers and digital signal processors (DSPs) changed how modern control systems are realized in hardware. While the classical control systems were implemented utilizing operational amplifiers and other analog hardware, today's modern controllers use software and digital processors to perform the required tasks. The controller realization in software increases the flexibility of the system significantly. For the design of digital controllers, two different methods are available. One way is to design the compensator as a continuous time system and then transforming it in the digital domain. The other way is to carry out all the design in discrete time. Since Section 3.2 gives a pole placement design method in the continuos time domain, the first technique was applied in this work. Attempts to perform a similar derivation as in Section 3.2 but in discrete time were not successful.

Digital position feedback control has experienced only brief reflections in the literature. To the authors knowledge, Fagan's work (1993) addressed issues of digital PPF filters at first. Others [McEver (1999); DeGuilio (2000)] used his results and applied it to structural vibration control. Kwak, Han, and Seoul (1998) also used digital PPF filters for their application of genetic algorithms.

This research employed a dSpace DSP board for the filter implementation and, therefore, required transformation of the continuous time filter equation (Equation (3.3)). The Tustin

transformation showed the best results in mapping the poles and zeros from the s-domain in the z-domain. Equation (3.27) presents the transformation, also known as trapezoid rule or bilinear transformation

$$s = \frac{2}{T}\frac{z-1}{z+1} \tag{3.27}$$

where T is the sampling time, s is the complex frequency in the Laplace domain, and z is the complex frequency variable in the discrete time domain. Substituting Equation (3.27) into Equation (3.3) results in the transformed PPF filter equation:

$$\begin{aligned} G_{PPF}(z) &= G_{PPF}(s)\Big|_{s=\frac{2}{T}\frac{z-1}{z+1}} \\ G_{PPF}(z) &= \frac{g\omega_f{}^2T^2(z^2+2z+1)}{(\omega_f{}^2T^2+4\zeta_f\omega_fT+4)z^2+(-8+2\omega_f{}^2T^2)z+(\omega_f{}^2T^2-4\zeta_f\omega_fT+4)} \end{aligned} \tag{3.28}$$

To keep the parameters flexible the filter could not be implemented as a complete transfer function. Instead, the canonical form, diagrammed in Figure 3.11, was used. Equation (3.29) gives the transfer function in canonical form. The actual realization in Simulink can be found in Appendix C.

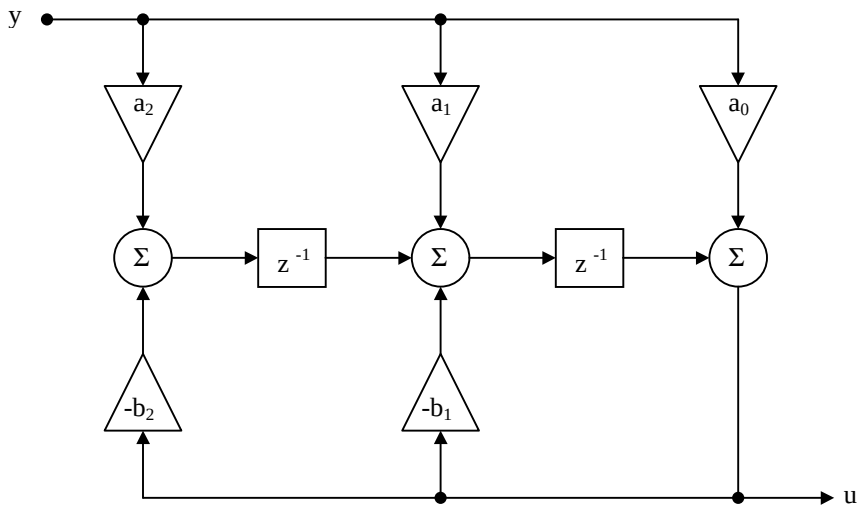

Figure 3.11. Canonical Form of Digital PPF Filter.

$$G(z) = \frac{a_2 z^{-2} + a_1 z^{-1} + a_0}{b_2 z^{-2} + b_1 z^{-1} + 1} \tag{3.29}$$

with:

$$a_0 = \frac{g\omega_f{}^2 T^2}{\omega_f{}^2 T^2 + 4\zeta_f \omega_f T + 4}; \quad a_1 = \frac{2g\omega_f{}^2 T^2}{\omega_f{}^2 T^2 + 4\zeta_f \omega_f T + 4}; \quad a_2 = \frac{g\omega_f{}^2 T^2}{\omega_f{}^2 T^2 + 4\zeta_f \omega_f T + 4}$$

$$b_1 = \frac{2\omega_f{}^2 T^2 - 8}{\omega_f{}^2 T^2 + 4\zeta_f \omega_f T + 4}; \quad b_2 = \frac{\omega_f{}^2 T^2 - 4\zeta_f \omega_f T + 4}{\omega_f{}^2 T^2 + 4\zeta_f \omega_f T + 4}$$

Equations (3.28) and (3.29) show that the digital PPF filter contains one more design parameter than the continuous time equivalent. While the continuous filter has the filter frequency ω_f, the filter damping ratio ζ_f, and the filter gain g, as parameters, the digital filter extends the parameter set through the sampling time T. As for all parameters there exists an optimal value for the sampling time given certain boundary conditions and restrictions. However, the determination of this optimal value is much more difficult than for the other three parameters. Indeed, to the authors knowledge, a closed form solution for the sampling time T does not exist. There are, however, a few rules of thumb which need to be considered.

First, there is the sampling theorem. The sampling theorem defines the lowest possible sampling frequency as $f_{s\ min} = 2\ f_{max}$, to avoid aliasing of the signals, where f_{max} is the highest occurring frequency. Since frequencies up to 400 Hz are considered on the experimental structure the sampling rate for this research can not be lower than 800 Hz. Nevertheless, the frequency $f_{s\ min}$, also known as Nyquist frequency, is generally not the best choice for active control systems. The slow sampling creates a phase lag in the signals, and therefore, influences the performance and the stability of the closed-loop system.

Another approach would be to sample as fast as possible. The limits here lay in the costs of the hardware. Faster analog to digital converter and DSPs are generally much more expensive than the devices with slower tact rates. Franklin et al. (1998) suggest a sampling frequency in the range of $20\ f_{max} < f_s < 40\ f_{max}$ for smooth performance, which means a sampling frequency of 8 to 16 kHz for the experiments. Those sampling rates, however, could not be achieved in the

experiments with the available hardware. Furthermore, sampling rates as high as twenty or forty times the structural frequencies do not seem to lead to optimal performance of positive position feedback filters.

To analyze the influence of the sampling rate on the performance a closed-loop system with a digital PPF filter in the feedback loop was simulated. The plant was the previously analyzed second-order system with one pole at 50 Hz. In the first simulation the frequency of the zero was varied from 50 to 75 Hz, which corresponds to the zero-pole ratio from ω_{zp} = 1 to 1.5. Using the zero-order hold (ZOH) transformation and different sampling rates, the structural plant was transformed into the z-domain. Applying the optimal filter parameters from Section 3.2 with a gain margin of 5, the PPF filter was Tustin-transformed with the same sampling rates as for the plant. The ratio of the maximum magnitude of the uncontrolled plant to the maximum magnitude of the controlled plant represents the performance of the controller. Figure 3.12 shows this ratio plotted versus the sampling rate and versus the zero-pole spacing. Notice that the general relationship between the increasing zero-pole spacing and higher performance is also valid for a digital filter. Notice in particular that there appears to be an optimal sampling frequency for each value of the zero-pole ratio. Whereas maximum damping for a small zero-pole ratio (ω_{zp}.= 1.075) occurs at f_s = 350 Hz for zero-pole ratios as high as 1.5 the optimal sampling frequency lays at 600 to 700 Hz. This corresponds to sampling frequencies 7 to 14 times the frequency of the structural pole.

To analyze the connection between performance, sampling rate and gain margin the second-order plant was simulated again. This time the zero-pole ratio was kept constant at 1.2. Figure 3.13 presents the performance of the controller depending on gain margin and sampling rate. It is interesting to note that there appears to be an optimal set of values for the sampling rate and the gain margin at 300 Hz and 2.8, respectively. Over the full range of the gain margin ($1.55 < GM < 5.8$) the sampling frequencies causing the best performance stretch out between 200 and 500 Hz. This corresponds to sampling frequencies 4 to 10 times the frequency of the structural pole.

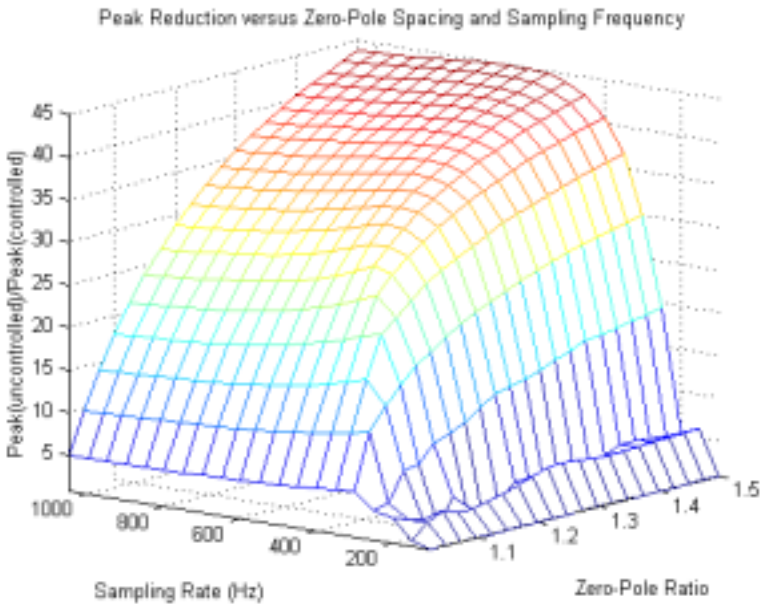

Figure 3.12. Ratio of the Maximum Magnitude of the Open-Loop System to the Maximum Magnitude of the Closed-Loop System versus Sampling Rate and Zero-Pole Spacing.

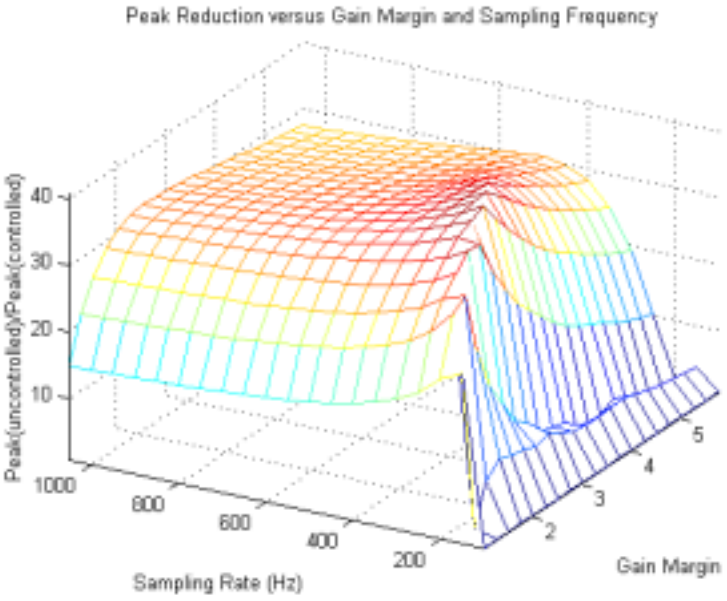

Figure 3.13. Ratio of the Maximum Magnitude of the Open-Loop System to the Maximum Magnitude of the Closed-Loop System versus Sampling Rate and Gain Margin.

The results of the simulations show that the optimal sampling rate for a PPF filter is a compromise influenced be many factors. As a rule of thumb it can be summarized that the sampling frequency for the plant and the filter should not be lower than four times the frequency of the pole. Furthermore, increasing the sampling frequency to over 14 times the pole frequency results in decreasing performance, and therefore, should be avoided. For the experimental tests, however, the situation was not so straight forward. The test specimen was a multi-mode structure with pole frequencies from 40 to 360 Hz. Choosing a sampling rate ten times larger than the frequency of the first mode would result in a violation of the sample theorem for the highest frequencies measured. Instead, sampling rates between 3.3 and 4 kHz were chosen which corresponds to a sampling factor of about 10 for the highest modes but of about 100 for the lowest mode.

In Section 3.2, a pole placement design was performed for the PPF filter in the Laplace domain. Thereby the complex plane with the pole and zero locations served also as a stability check. As long as all poles remained in the left half plane, stability was ensured. Since the Tustin transformation maps all points from the left half plane in the unit circle in the z-domain, all poles of a discrete time system have to remain inside the circle. To test how the optimal pole locations from Figure 3.8 map into the z-domain a root locus analysis for the digital closed-loop system was performed. The parameters for the plant remained the same and for the digital filter the results from the previous paragraphs are used. That means the sampling rate was set to 300 Hz and the gain margin was fixed at 2.8 for the second-order plant with a zero-pole spacing of 1.2. Figure 3.14 shows the pole-zero map of the closed-loop system. Note that poles with equal damping in the z-domain lie on logarithmic spirals compared to straight lines in the Laplace domain. Although the structural pole and the filter pole were designed to have the same damping ratio in continuous time, the poles in the graph do not lie on the same spiral. It is interesting to observe that the parameters, which lead to the digital PPF filter with the best performance, result in closed-loop poles with different damping ratios. The pole-zero map in Figure 3.14 also shows the open-loop pole of the plant. Notice its location on the border of the unit circle with almost no damping.

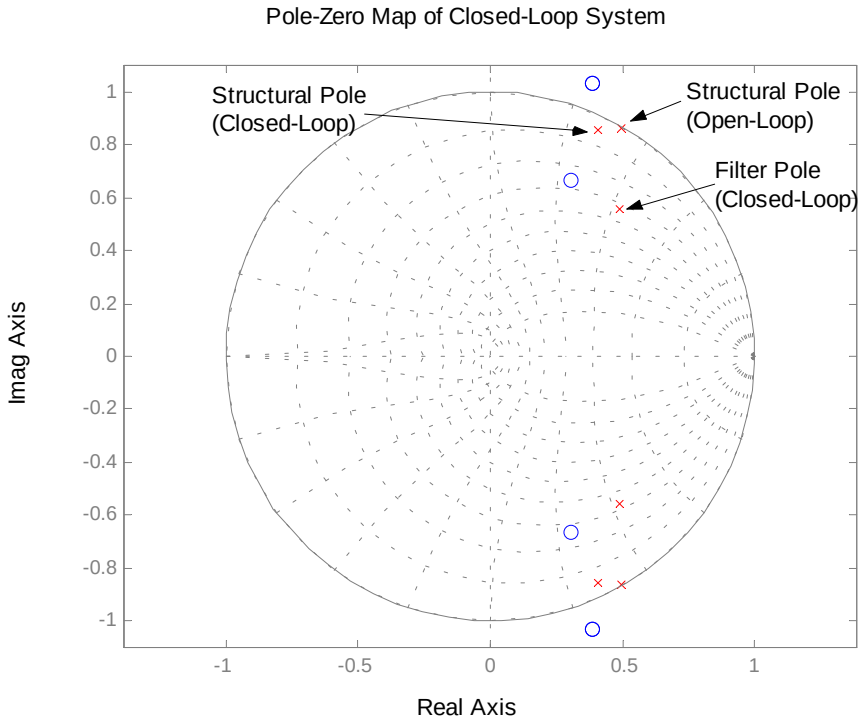

Figure 3.14. Pole-Zero Map of the Open-Loop Plant and the Closed-Loop System with Optimal PPF.

To understand the different behavior of the digital system compared to the continuous time system the effects of the ZOH transformation on the plant were investigated. Figure 3.15 presents the frequency response function of the digitized plant in relation to the continuous time plant. Surprisingly, the zero-order hold transformation appears to change the frequency response of the second-order system significantly. While the pole of the system gets transformed correctly using a sampling rate of 300 Hz, the transformed zero does not affect the magnitude of the response in the wanted manner. As it can be seen in the right half of Figure 3.15, faster sampling improves the matching of the discrete response but frequencies above 8kHz are needed to match the magnitude curve exactly. To match the phase curve more accurately sampling rates above 14.398 kHz are necessary for the chosen example. Those frequencies, however, would exceed hardware limitations and are only of theoretic nature.

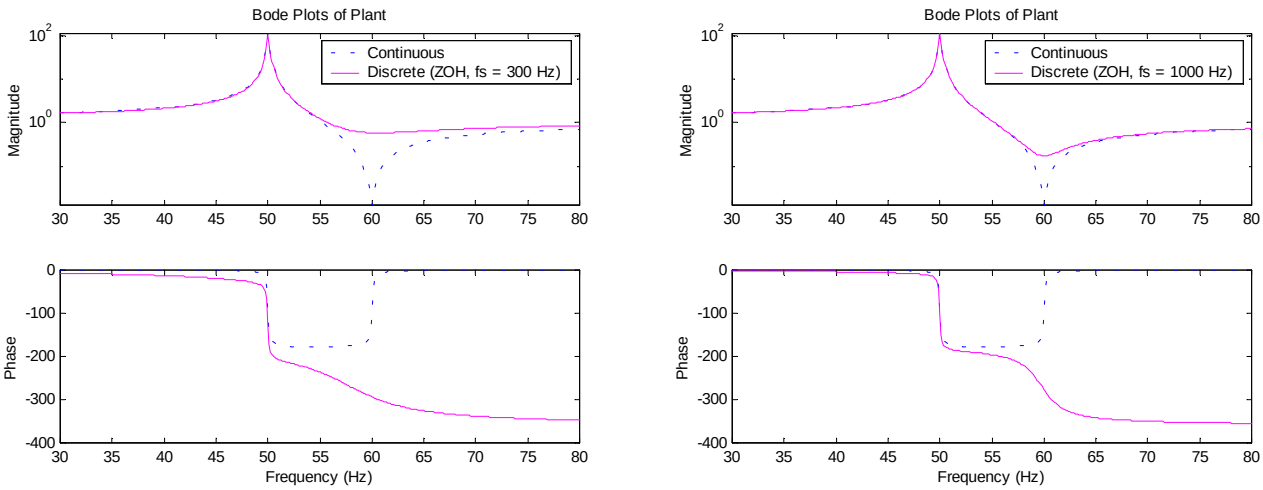

Figure 3.15. Frequency Response of ZOH-Transformed Plant (Right: f_s = 300 Hz, Left: f_s = 1000 Hz) Compared to the Continuous Time Frequency Response.

Although that fact of different behavior of the digital system can be explained by the effects of the zero-order hold transformation, the quantitative evaluation is not part of the objectives of this research.

3.4 Summary

This chapter has presented the theory behind positive position feedback (PPF) control. The use of PPF controllers for structural vibration control have been discussed. The derivation of optimal PPF parameters showed that the maximal amount of closed-loop damping added by a PPF filter depends on the spacing of the pole frequency to the zero frequency in the collocated transfer function of the structure. The last part of this chapter addressed issues of the digital PPF filter. The analysis of the most suitable sampling rate for filter and plant has demonstrated that the fastest possible sampling rate does not necessarily lead to the best performance of the active vibration damping. The effects of the zero-order hold transformation proved to influence the performance as well.

Chapter 4

Experimental Setup and Baseline Tests

This chapter describes the experimental setup used in this research. First, the mechanical design of the vibration test stand is presented. The second section gives an overview of the hardware used. The placement of the actuators and sensors is discussed as well as signal conditioning circuits and the data acquisition system. The last part of this chapter documents the baseline tests performed to determine the best sensor actuator combination to fulfill the objectives of this research.

4.1 Test Stand Design

The test stand used for the experiments in this research was originally designed for analyzing and testing the effectiveness of passive and active damping materials for reducing structural vibration and the resulting noise. The test stand provides clamped-clamped boundary conditions for the test plates representing an automotive or aircraft structure. Equipped with data acquisition systems for acoustic and vibration data the test stand enables the comparison of different smart material damping techniques as well as standard damping materials such as carpeting and passive damping materials. The test plate, clamped rigidly on all four edges, can be excited through an electromagnetic shaker over various frequency ranges. Figure 4.1 shows the VTS g100-6 100-lb shaker in its operating position.

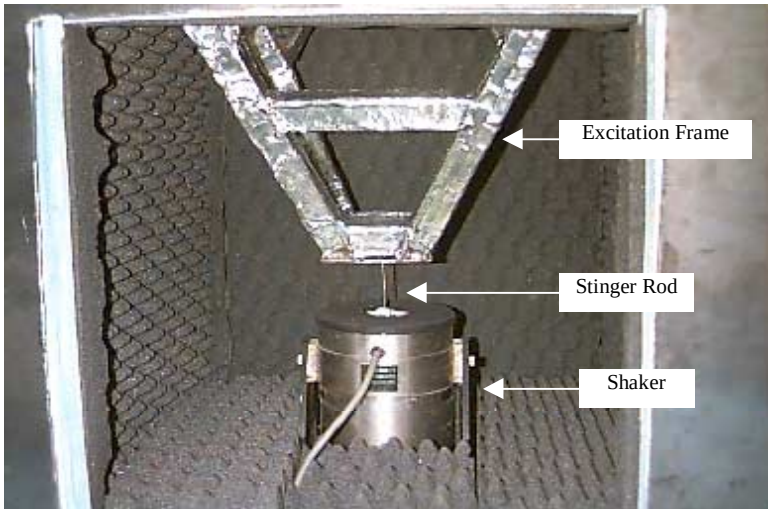

Figure 4.1. Electromagnetic Shaker and Stinger Rod Assembly [Jeric, 1999].

The standard test plate used on the test stand is a 20 gauge galvanized steel plate with dimensions of 500 mm × 600 mm. To ensure repeatable boundary conditions the 14 clamping bolts were always tightened in the same criss-crossing pattern to a torque of 25 Newton-meter (20 foot-pounds). By clamping the plate in the excitation frame, the effective area of the plate is reduced to 400 mm × 500 mm. Figure 4.2 shows the test plate mounted in the frame. The edge area around the clamping frame was covered with an acoustic barrier for the tests.

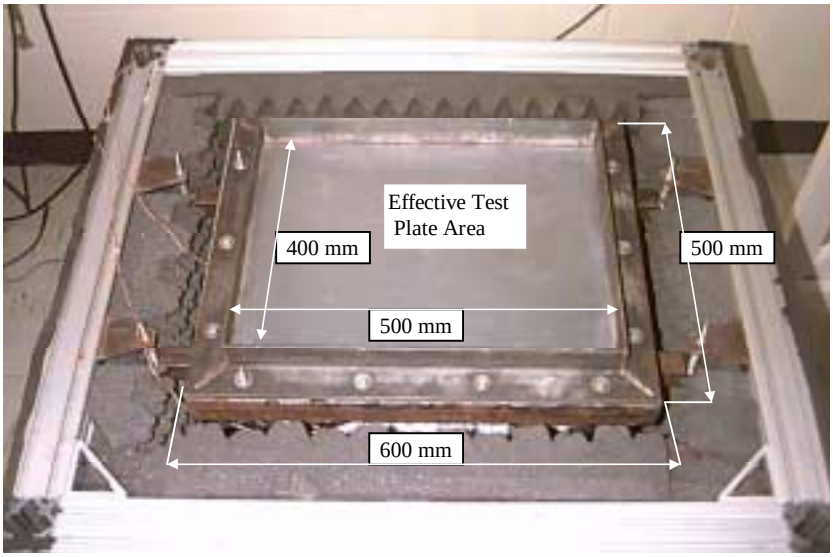

Figure 4.2. Standard Test Plate in Testing Position [Jeric, 1999].

To allow vertical vibrations of the plate the excitation frame is supported by four suspension springs. The design of the springs ensures that the dynamics of the suspended frame do not interfere with the dynamics of the test specimen. For acoustic measurements, the test stand also includes a top enclosure. However, the top enclosure was not used in this research because no acoustic data were taken. For details on the test stand design, the interested reader may be referred to [Jeric, 1999].

4.2 Test Setup

4.2.1 Test Plate Setup, Actuator, and Sensor Locations

The development of a "smart" material damping technique requires the choice and placement of sensors and actuators. As in previous studies on the test stand [Jeric (1999), DeGuilio (2000)] this research uses piezoelectric ceramic (PZT) patches as actuators. These actuator patches are commercially available and have the dimensions 72.4 mm × 72.4 mm × 0.267 mm (2.85" × 2.85" × 0.0105"). More information about the properties of these actuators can be found in Appendix E. To minimize the weight added by the smart material only one actuator was used in this research.

Because the objective of this research was to increase the damping of the first three to four vibration modes, the PZT actuator was placed in the center of the plate. DeGuilio (2000) showed in his work that the center location provides enough control authority over the lower frequency modes. His results and a finite element model of the test specimen (Appendix A) were considered to choose that location. Figure 4.3 presents a diagram with the measures of the PZT placement.

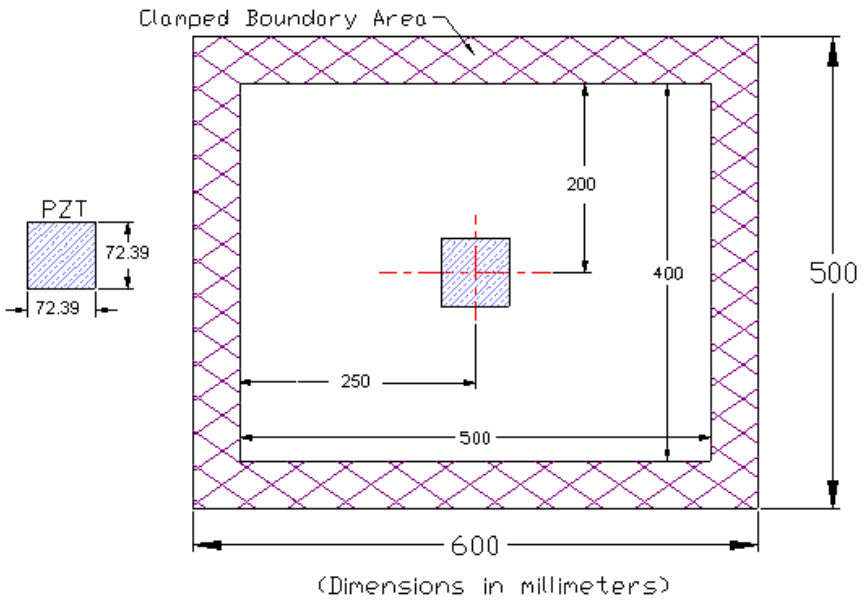

Figure 4.3. PZT Placement on the Test Plate [DeGuilio, 2000].

To attach the ceramic patch to the plate, the surface of the plate was first sanded and then cleaned with alcohol and a wiping cloth. A commercially available glue containing cyanoacrylate ester, for instance "Super Glue" served as an adhesive. To ensure proper bonding of the ceramic to the steel plate, the joint was loaded with equally distributed weight for about one hour. Soldering a wire lead to the upper electrode of the PZT made one electrical contact. Due to the conductive bond properties of the cyanoacrylate adhesive, the steel plate and lower electrode of the patch became automatically connected. Figure 4.4 shows the piezoelectric ceramic patch in place.

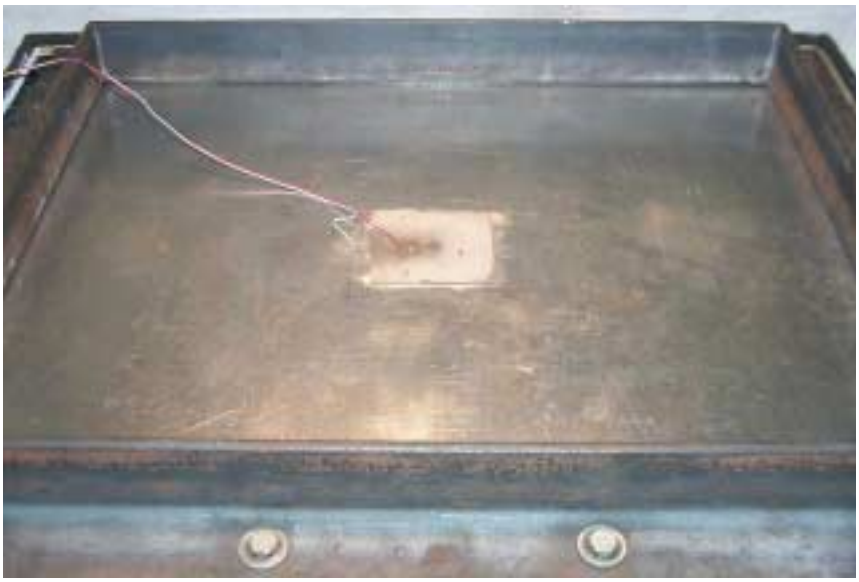

Figure 4.4. PZT Bonded to the Surface of the Test Plate.

In contrast to the study undertaken by DeGuilio, this research relies on conventional accelerometers and PZTs as sensors. The optical strain sensors used in his work showed some unpredictable property changes during the testing due to the linearization process of the sensor signal. Those property changes, which occurred even more often when the temperature was varied, were intolerable for the automated control system investigated here. The first choice for a sensor was a PZT patch, similar to the actuator PZT but with smaller dimensions (20 mm $\times$ 20 mm $\times$ 0.267 mm). Attaching the sensor PZT into the center of the lower side of the testing plate in the same manner as the actuator created the required collocated sensor/actuator system. Another type of sensor, an accelerometer was also attached into the center of the test plate. The accelerometer Model 333A from PCB Piezotronics Inc., fastened to the plate with a drop of adhesive from a glue gun, provided an alternative vibration signal. Information about the specification of the accelerometer can be found in Appendix E. The advantages and disadvantages of both sensors types will be examined and discussed in Chapter 4.3. Figure 4.5 shows all sensors in the center of the bottom side of the plate. The picture also shows the accelerometer used for the data acquisition system and a second PZT sensor slightly out of the center.

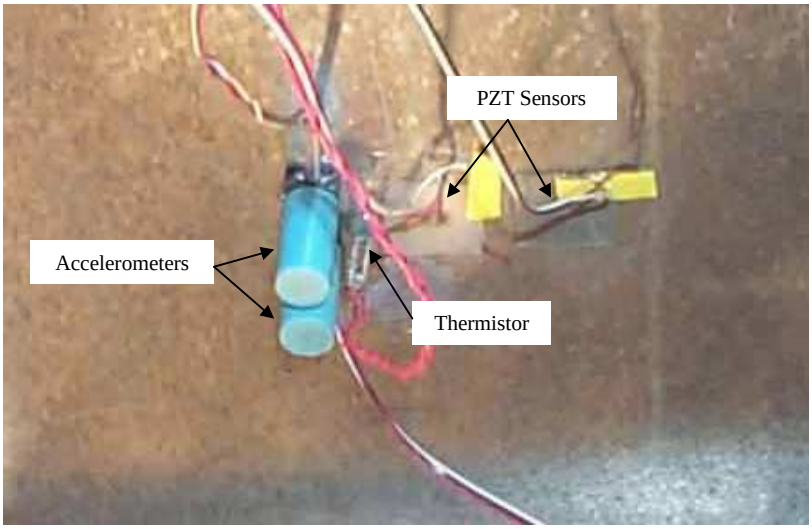

Figure 4.5. PZT Sensors and Accelerometers on the Bottom Side of the Plate.

One of the challenges in this project was to show that active vibration control is possible under varied temperatures. Therefore, a heat source was required. Emitting infrared radiation a 250 W heat lamp, placed about 30 cm (12 in) above the plate, was able to heat the center of the plate up to 70°C (160°F). To measure the temperature a 10kΩ-thermistor was attached to the plate. Whereas the thermistor can be seen in Figure 4.5, Figure 4.6 shows the overall setup with heat lamp and signal conditioning circuits. Due to the location of the heat lamp over the center of the plate the distribution of the heat was not very uniform. While the highest temperature was always reached in the center, the temperature decreased significantly towards the boundaries of the plate.

Figure 4.6. Overall Setup with Heat Lamp and Signal Conditioning Circuits.

4.2.2 Signal Conditioning

Due to the use of a digital signal processor (DSP) to realize the positive position feedback filter, a conversion of the digital signals coming from the compensator to analog signals for the actuator was necessary. Implemented in the DSP board, a common 12-bit digital to analog (D/A) converter performed this task. Because of the zero-order-hold design of the D/A converter the resulting signal looked like a staircase signal and, hence, contained unwanted higher frequencies. With a cut off frequency of about 500 Hz and a gain of one, the Sallen-Key low pass circuit operated as a smoothing filter. The circuit diagram of the filter and the values of its components are shown in Figure 4.7. Equation (4.1) gives the transfer function of the second-order filter [Hevey, 1998].

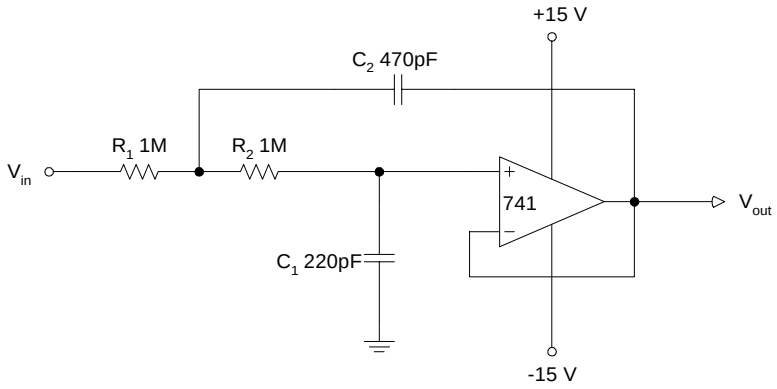

Figure 4.7. Smoothing Filter for D/A Converter Output.

$$G_{LP}(s) = \frac{V_{out}(s)}{V_{in}(s)} = \frac{1}{R_1 R_2 C_1 C_2 s^2 + C_1(R_1 + R_2)s + 1} \tag{4.1}$$

To adjust the high output impedance of the piezoelectric sensor to the lower input impedance of the analog to digital (A/D) converter of the digital signal processor board a buffer circuit was used. The buffer circuit also works as a high pass filter with the cut-off frequency of about 0.1 Hz. That way, the circuit can counter DC shifts in the sensor signal, which can occur due to the high sensitivity of the PZT sensor to very low frequencies [Hevey, 1998]. The values for the components were chosen such that the filter gain remained equal to one in the frequency range of operation. The selected operational amplifier LF356, a J-FET type, is characterized by a very high input impedance (10^{12} Ω) and therefore is very suitable for this application. While Figure 4.8 presents the circuit diagram of the high pass filter Equation (4.2) gives the transfer function. Note that the capacity of the sensor PZT (C_{PZT} = 28 pF) has to be taken into account for the calculations.

The PCB signal conditioner (584 Series), available from PCB Piezotronics Inc., performed the conditioning of the accelerometer signal. The internal amplifier gain was set to 10. To increase the voltage on the actuator PZT a power amplifier from Trek Inc. (Model 50/750) was used. Figure 4.9 shows all equipment and parts used in the sensor to actuator chain.

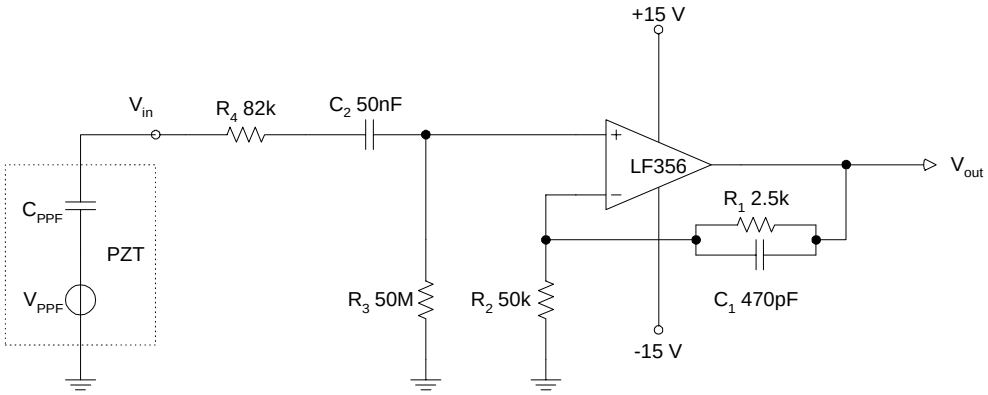

Figure 4.8. PZT Sensor Buffer Circuit.

$$G_{HP}(s) = \frac{V_{out}(s)}{V_{PZT}(s)} = \frac{C_1 C_{PZT} C_2 R_1 R_2 R_3 s^2 + C_{PZT} C_2 R_3 (R_1 + R_2) s}{C_1 C_{PZT} C_2 R_1 R_2 (R_3 + R_4) s^2 + [C_{PZT} C_2 R_2 (R_3 + R_4) + C_1 R_1 R_2 (C_{PZT} + C_2)] s + R_2 (C_{PZT} + C_2)} \quad (4.2)$$

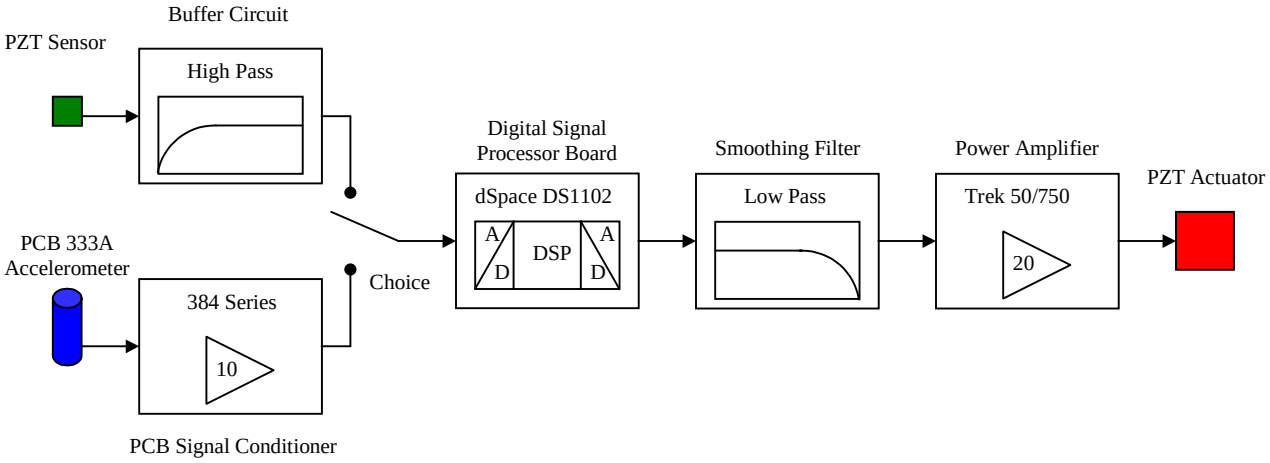

Figure 4.9. Equipment Overview, Sensor to Actuator Chain.

4.2.3 Data Acquisition System

The objective of the active control tests was to improve the vibration suppression in a representative aircraft panel. To measure the performance of the active control system, a data acquisition system was needed. The two-channel HP Dynamic Signal Analyzer 35665A became the heart of the data acquisition system. Using two PCB 333A accelerometers, the signal analyzer measured the frequency response function between the excitation frame and the plate. One of the accelerometers was placed on the frame and the other one was mounted on the bottom center of the plate together with the sensors for the active control system. Figure 4.10 shows the accelerometer on the excitation frame and the accelerometers and sensors in the center of the plate. Each of the two data acquisition accelerometers connected through the PCB 584 Series Signal Conditioner to one of the channels of the HP Signal Analyzer.

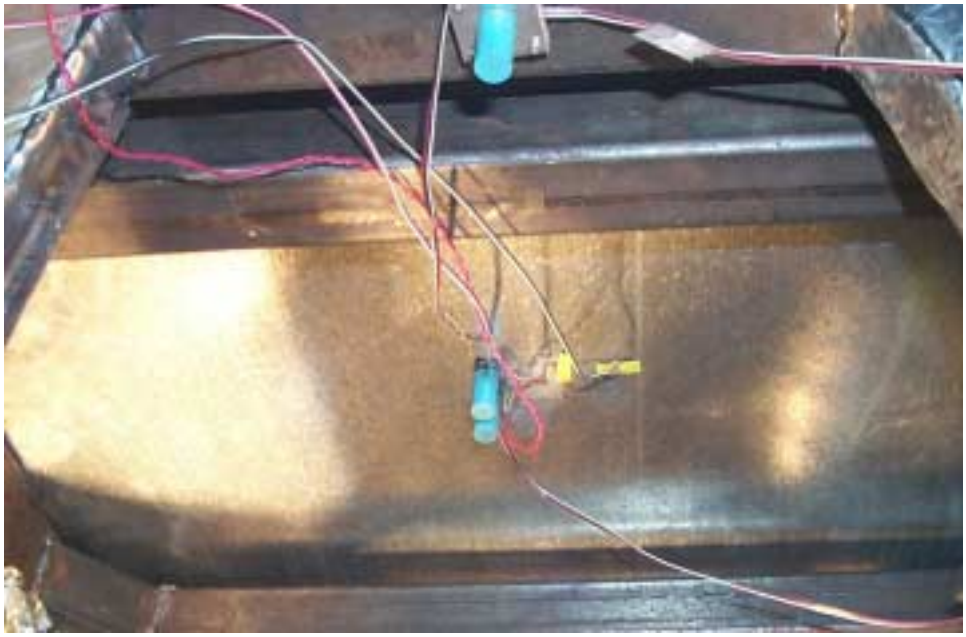

Figure 4.10. Accelerometers on the Excitation Frame and on the Bottom Side of the Plate.

The Dynamic Signal Analyzer was also used to generate the excitation signal for the shaker. For most of the tests, a periodic chirp signal with an amplitude of 250 mV (rms) was chosen. To drive the VTS g100-6 100-lb shaker the source signal from the HP was amplified

through the Techron 5330 Power Amplifier. Figure 4.11 presents the data acquisition elements. The terminology frequency response function of the plate will refer to data taken with those elements throughout this work.

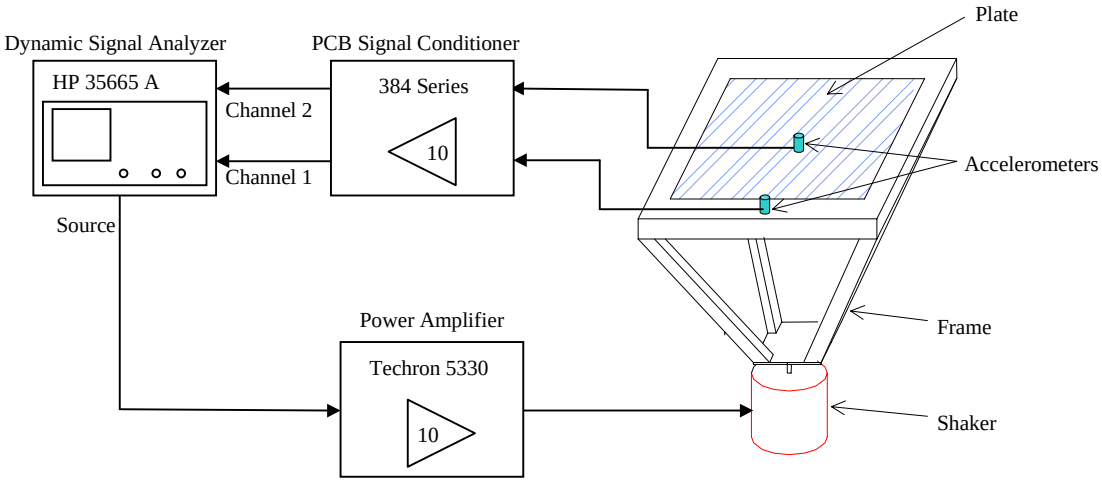

Figure 4.11. Data Acquisition System.

4.3 Baseline Tests

The purpose of the baseline tests was to examine the influence of the increased temperature on the plate and on the sensor/actuator pair. Using a dimmer in the power cord of the heat lamp, the temperature in the center of the plate could be increased in 2.5°C steps from room temperature up to 65°C (150°F). The frequency response function of the plate was taken every time a steady state of the desired temperature was reached. Figure 4.12 shows the transfer function of the undamped plate at two different temperatures. Note the significant change in the frequency response of the test specimen at increased temperature. The first vibration mode shifted from about 50 Hz at room temperature to over 100 Hz at 65°C (150°F). The author believes that the extreme change in the properties of the plate is due to mechanical strain and tension in the plate induced by a temperature gradient over the plate area. The infrared lamp, located over the center of the test specimen, hardly increased the temperature on the edges of the plate or on the

clamping frame itself. Therefore the thermally induced material expansion remained mainly in the center part and even caused the plate to warp out at temperatures as high as 65°C (150°F). For later experiments, the temperature was kept below 45°C to avoid the extensive bending stress for the structure and the smart materials. The effects of the temperature changes on the plate were already noticed by [DeGuilio, 2000] and mainly drove the idea for this research.

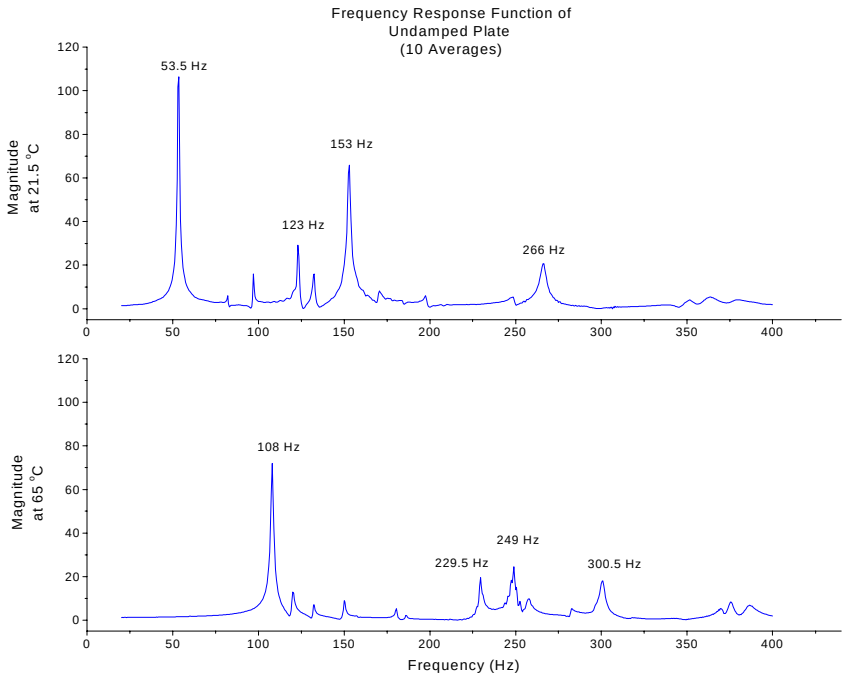

Figure 4.12. Frequency Response of Plate at 21.5°C (70°F) and 65°C (150°F).

As shown in Chapter 3 the optimal parameters for the positive position feedback filters depend on the zero/pole spacing of the structural transfer function. Hence, the exact determination of the zero and pole frequencies of the structure is essential. Two different types of sensors are analyzed for that purpose. The first choice was a piezoelectric sensor in conjunction with the signal conditioning circuit described in the chapter before. Together with the PZT actuator, this sensor established the classical collocated sensor/actuator pair. To test whether the structural poles and the sensor location zeros could be found with the PZT-

sensor/PZT-actuator pair the test setup shown in Figure 4.13 was used. Note that instead of the electromagnetic shaker the piezoelectric actuator exited the plate for this experiment.

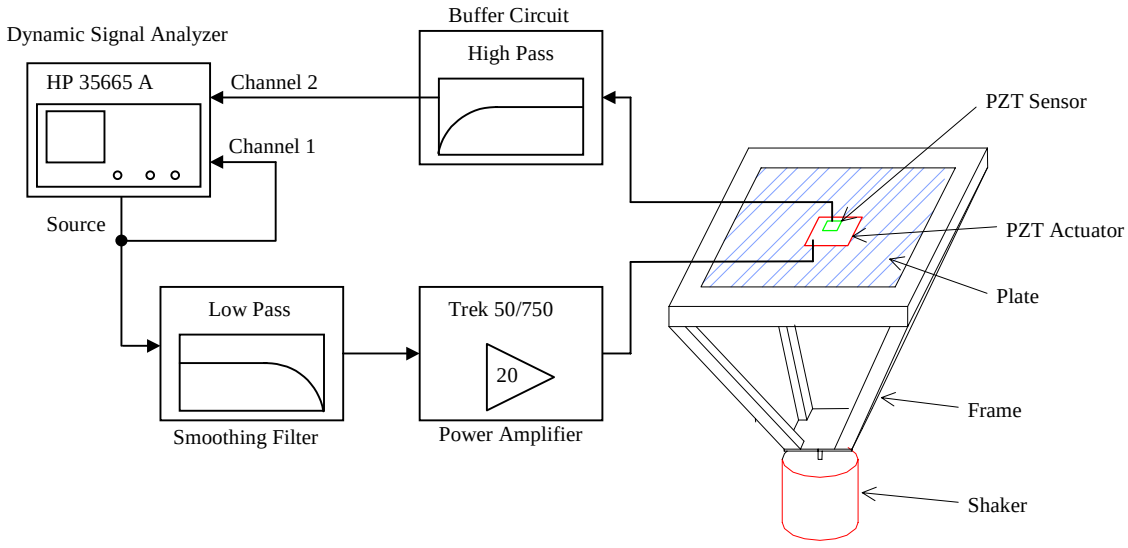

Figure 4.13. Experimental Setup for Measuring the Collocated Transfer Function (PZT → PZT).

Although the amplitude of the first pole is very low, the collocated transfer function agreed sufficiently with the frequency response of the plate at room temperature. Surprisingly however, at increased temperatures the lower vibration modes start to vanish completely due to pole/zero cancellations. Figure 4.14 shows this effect comparing the collocated transfer function to the frequency response of the plate at two different temperatures. The observed pole/zero cancellations imply that those certain vibration modes are uncontrollable with the used sensor/actuator system. The author also tried slightly de-centered sensor locations on the plate, but without any improvements for the controllability. Hence, the PZT-sensor/PZT-actuator combination had to be rejected. The objectives of this research, the increase of the damping ratio in the lowest three to four vibration modes could not be achieved using a piezoelectric sensor.

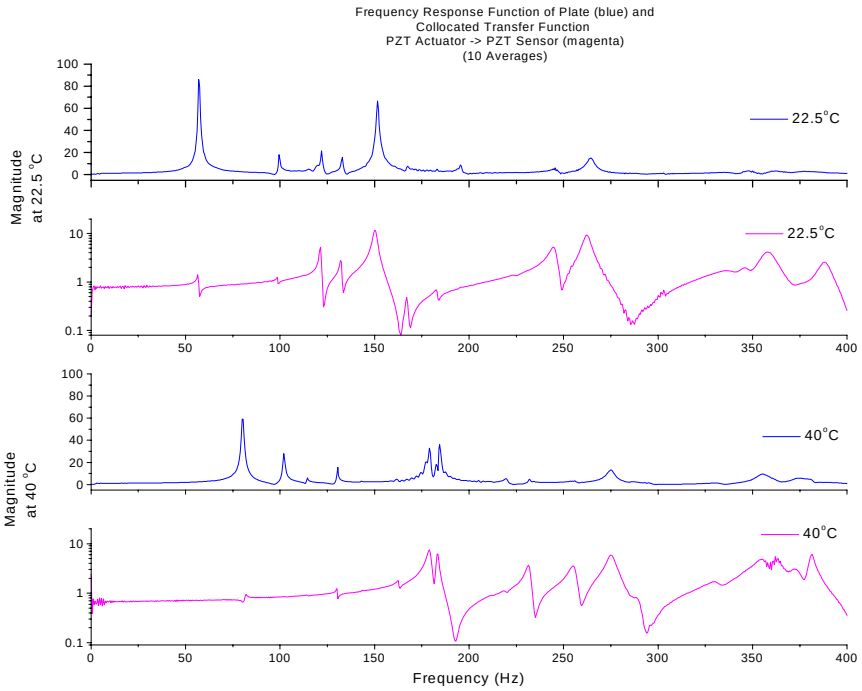

Figure 4.14. Frequency Response of Plate and Collocated Transfer Function at 22.5°C (72°F) and 40°C (104°F)..

As a second choice, an accelerometer was considered as a vibration sensor. Located in the center of the test specimen the PCB 333A accelerometer provided a displacement to acceleration collocated transfer function together with the PZT actuator. Due to the need of a displacement sensor signal for the positive position feedback controller, a double-integrator was implemented in the DSP board. The integrator was designed as a pseudo-integrator having one zero at 0 Hz and an extra pole at 5 Hz to counter the effects of the zero. The use of a regular integrator would have caused the integration signal to increase up to the saturation limits of the DSP at the slightest DC offset in the sensor signal. To analyze the properties of the new sensor/actuator pair a similar test setup was used as for the PZT-sensor/PZT-actuator pair. While Figure 4.15 presents the setup, Figure 4.16 shows the results. The results clearly indicate that the accelerometer/PZT-actuator combination is able to detect all vibration modes of interest over the temperature range. Therefore, the accelerometer will serve throughout this work as a sensor.

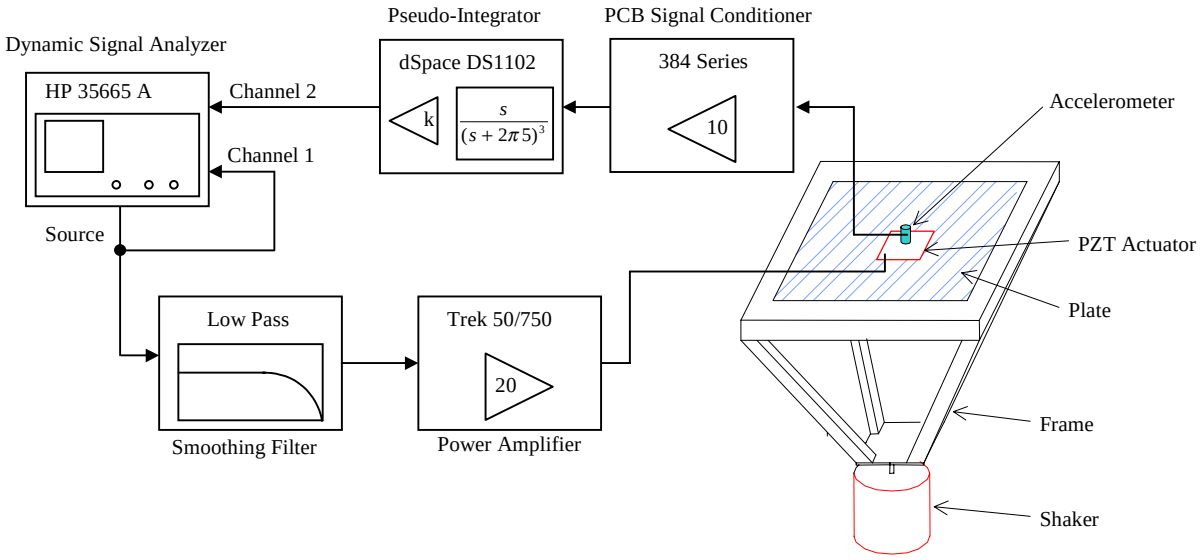

Figure 4.15. Experimental Setup for Measuring the Collocated Transfer Function (PZT → Accelerometer).

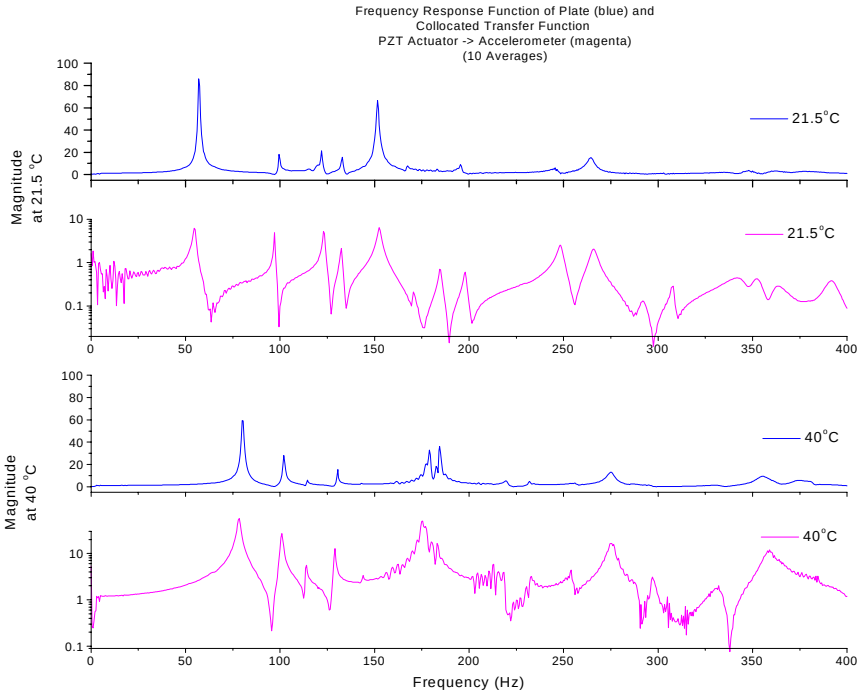

Figure 4.16. Frequency Response of Plate and Collocated Transfer Function (PZT → Accelerometer) at 22.5°C (72°F) and 40°C (104°F).

Chapter 5

Parameter Adaptation through Temperature Measurement

This chapter describes one approach for an active vibration control system using three PPF filters in parallel. Due to the property changes of the test plate under varying temperatures the parameters of the PPF filter had to be adjusted in order to attain vibration suppression over the temperature range from 20°C (68°F) to 40°C (104°F). Using a lookup table the parameter could be adjusted according to the current temperature. The chapter also presents active vibration control results achieved with this approach.

5.1 Algorithm

As mentioned in Section 4.3 the pole and zero frequencies changed significantly with an increase in the plate temperature. To clarify the relationship between resonance frequencies and plate temperature the collocated transfer function between the PZT actuator and the accelerometer was measured for temperatures between 17.5°C (63.5°F) and 45°C (113°F) in 2.5°C (4.5°F) increments. Figure B1 in Appendix B presents this set of transfer functions for different temperatures. The frequencies of the five major resonance modes are plotted in Figure 5.1 versus the plate temperature. Note that the different modes show different behavior with rising temperature. While the frequency of the first mode appears to increase monotonically the other modes show first a decreasing in frequency before increasing at higher temperatures. The problem now was to design an active vibration controller with positive position feedback (PPF) filters, which adapt to the changes in natural frequency due to temperature changes. The active controller described here employed an open-loop or gain scheduling adaptation process.

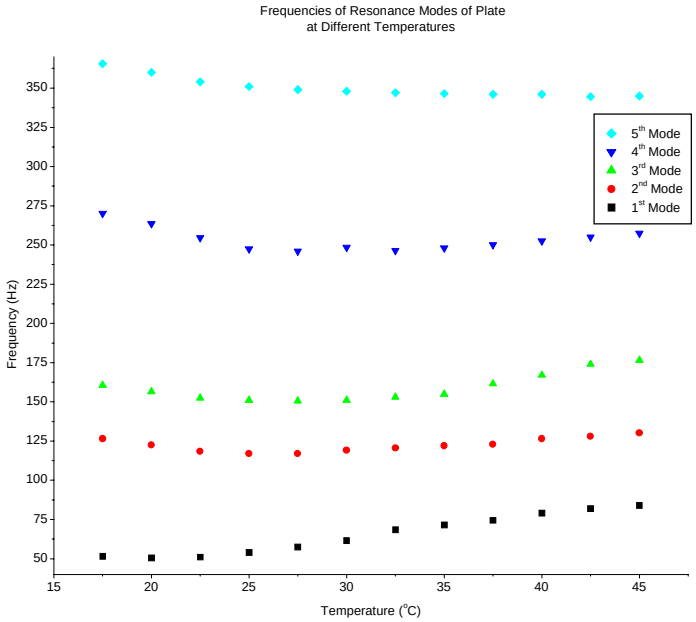

Figure 5.1. Resonance Mode Frequencies versus Plate Temperature.

Since the frequency changes of the test specimen appeared to be directly related to the temperature it was only reasonable to use a measurement of the temperature to adapt the controller parameters. The thermistor on the plate provided information about the temperature in form of its changing resistance. Using a voltage divider circuit as shown in Figure 5.2 the current thermistor resistance was computed with the voltages V_1 and $V(T)$. Equation (5.1) presents the dependencies. To calculate the actual temperature from the resistance of the thermistor the nonlinear characteristic was interpolated with a fifth-order polynomial. The polynomial coefficients and the thermistor specifications can be found in Appendix E.

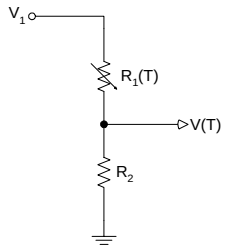

$$R_1(T) = R_2\left(\frac{V_1}{V(T)} - 1\right) \tag{5.1}$$

Figure 5.2. Voltage Divider Circuit with Thermistor.

Channel 3 of the digital to analog (D/A) converter of the dSpace system served as a constant voltage source for voltage V_1. The current value of the temperature was calculated within Simulink/dSpace, and therefore, was available for further usage in the algorithm. Figure 5.3 shows the temperature measurement subsystem in Simulink. The function block on the right side of the figure incorporated the fifth-order polynomial.

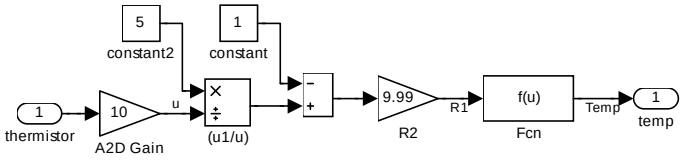

Figure 5.3. Temperature Measurement Subsystem in Simulink.

Stored in a Matlab script file, the information about the pole and zero frequencies was used to calculate optimal PPF filter parameters as derived in Chapter 3 for the modes to be damped at each temperature step. File D1 in Appendix D shows the M-file with the pole and zero frequencies and with the equations from Section 3.2. To link the current temperature to the optimal filter parameters, look-up tables were created for the Simulink/dSpace system. Figure 5.4 presents the Simulink model of the active controller with three PPF filters and the look-up tables. For temperatures between the 2.5°C increments, Simulink interpolates the output of the tables linearly. Double-clicking the rectangle in the lower part of the model caused the file *"adapt_init.m"* (Appendix D) to be executed and initialized the sampling time, the integrator parameters and the look-up tables. After compiling and downloading the model to the digital signal processor (DSP) the controller worked autonomously and adjusted the filter parameters g, ω_f, and ζ_f according to the measured temperature. Section 5.2 presents the vibration suppression results for this controller.

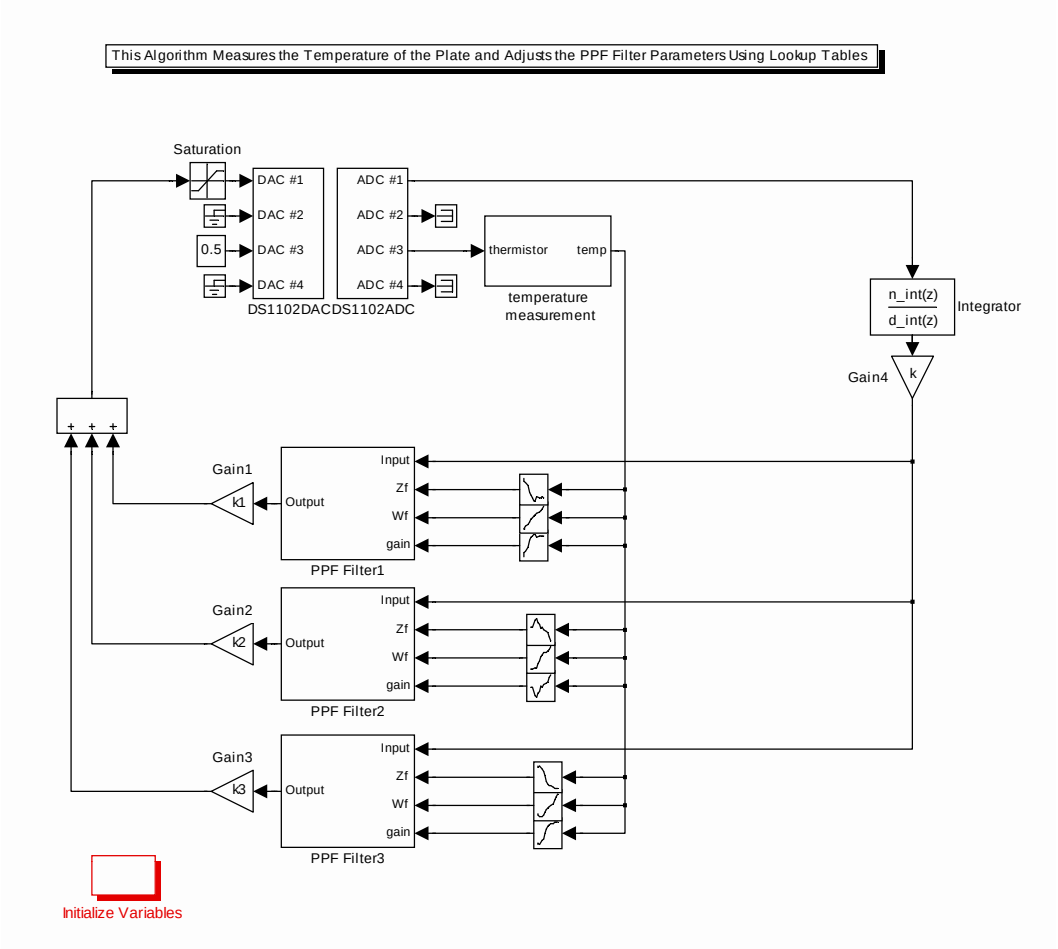

Figure 5.4. Simulink Model of Active Vibration Controller with Temperature Measurement.

5.2 Results

This section presents the vibration suppression results using the open-loop adaptation algorithm as described in Section 5.1. The gain margin for the parameter calculation was set to five and the sampling rate to 4 kHz. After the controller model from Figure 5.4 was compiled and downloaded to the digital signal processor (DSP) board the code execution on the DSP started automatically and the active controller began working. Using the test setup as shown in Figure 4.11 the frequency response function of the plate was measured for different temperatures starting at room temperature. Figure 5.5 compares the frequency response of the uncontrolled

plate to the response with the controller activated. The graph also shows the resonance mode frequencies for each temperature step. Notice the shift in the mode frequencies as the temperature rises.

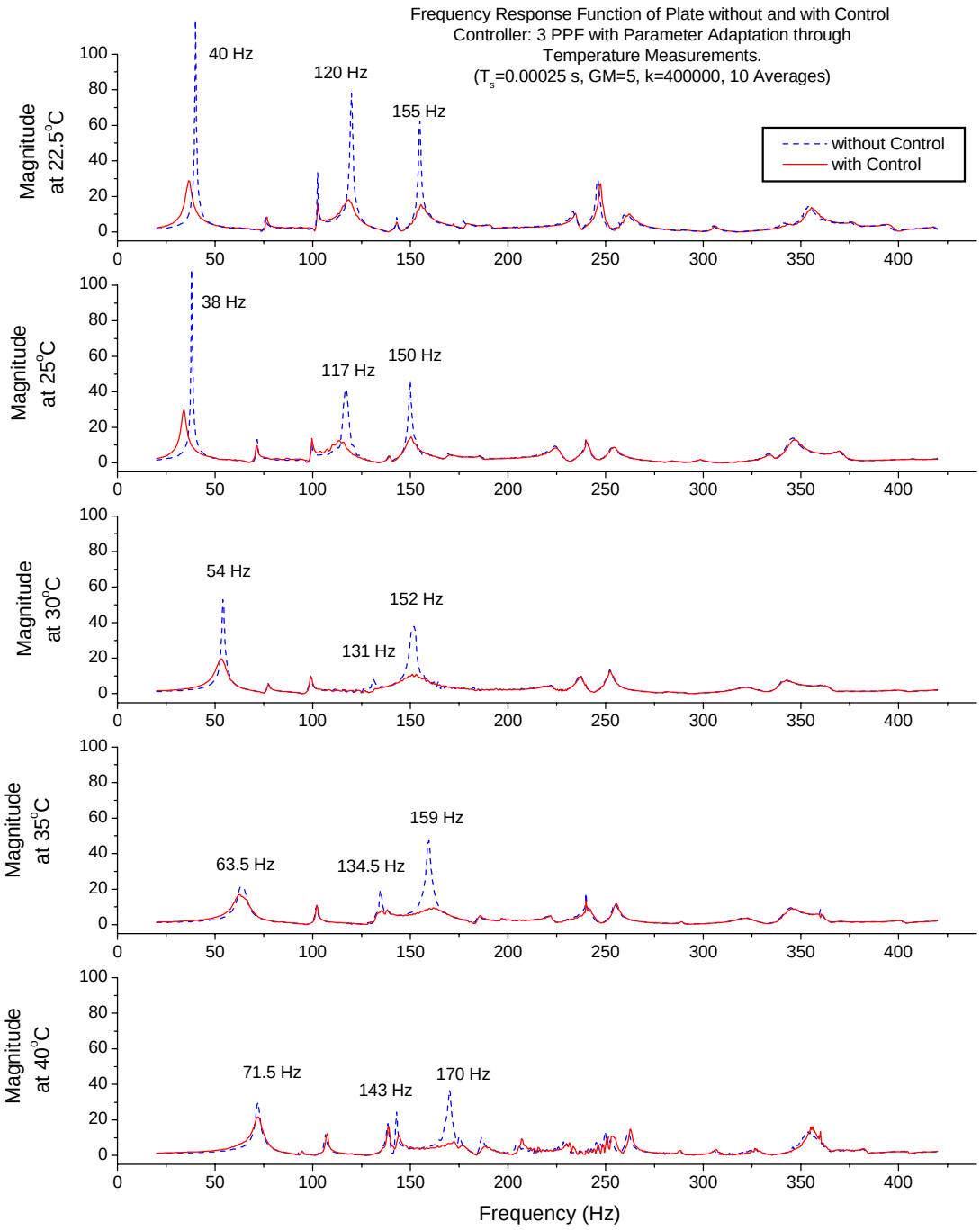

Figure 5.5. Frequency Response Function of Plate without and with Active Control at Different Temperatures.

Tests have shown that the best vibration suppression results can be achieved with one PPF filter tuned to the first mode (38 Hz to 71.5 Hz), one PPF filter tuned to the third mode (150 Hz to 170 Hz), and the third PPF filter tuned to the resonance mode around 350 Hz but with a gain reduced by a factor of 0.4. Notice in Figure 5.5 that tuning one PPF filter to the third resonance mode also decreased the magnitude of the second peak significantly, although none of the filters were adjusted to this mode. Tuning the third PPF filter to resonance mode around 350 Hz avoided an increase of the magnitude of the vibration modes at around 250 Hz and 350 Hz, which occurred if only two PPF filters were used. The reduced filter gain was necessary to keep the actuator signal in the limits of ±60 volts. Figure 5.6 shows the phenomenon where the use of only two PPF filters actually increased the amplitude of the higher frequency vibration modes.

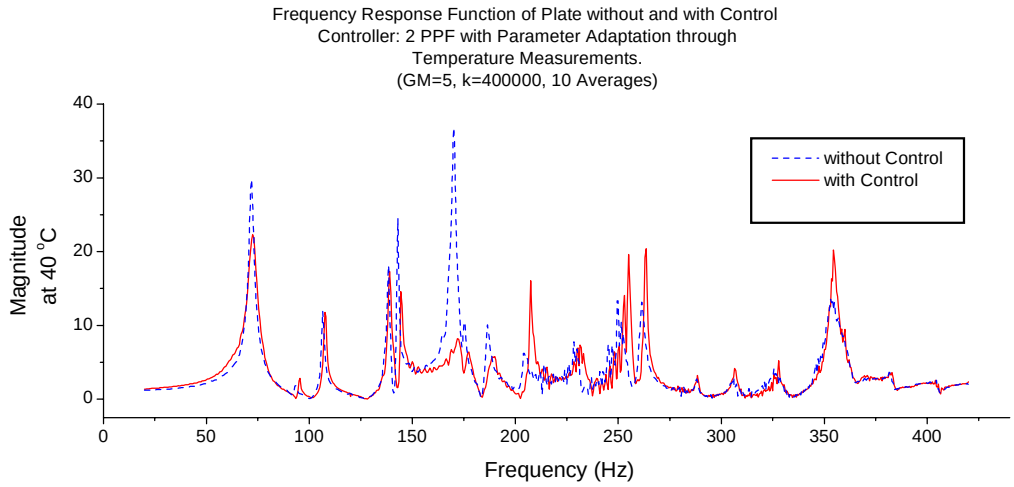

Figure 5.6. Frequency Response Function of Plate without Control and with two PPF Filters at 40°C (104°F).

The frequency responses of the plate in Figure 5.5 show that three PPF filters with open-loop parameter adaptation reduced the magnitude of the resonance peaks sufficiently, especially for temperatures up to 30°C (86°F). For higher temperatures, the PPF filter could not reduce the magnitude of the first mode significantly. The reason is that the zero, following the first mode pole, moves towards this pole and therefore decreases the pole-zero spacing $\omega_{zp} = \omega_z / \omega_p$. As derived in Section 3.2, the pole-zero spacing determines the maximum amount of damping, which can be added by PPF filters. Figure 5.7 compares the collocated transfer function,

measured between the PZT actuator and the accelerometer, at room temperature to the collocated transfer function at increased temperature. Whereas the pole and the zero of the first mode are very distinct in the upper half of the diagram, the pole and zero of the first mode almost cancel each other out in the lower half, decreasing ω_{zp} to nearly one.

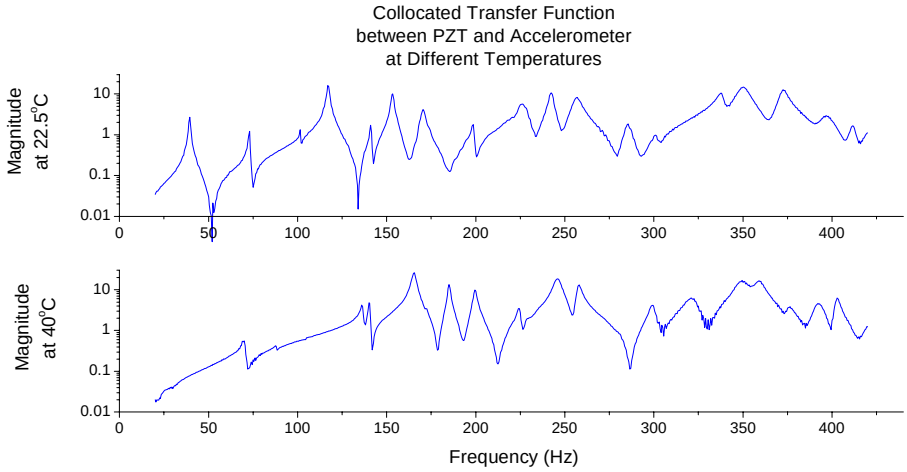

Figure 5.7. Collocated Transfer Function of Plate at 22.5°C (72.5°F) and 40°C (104°F).

To summarize the results, the magnitudes of the most significant resonance peaks of the uncontrolled plate are compared to the magnitudes of the same resonance peaks of the controlled plate in Table 5.1. Table 5.1 also gives the peak reduction ratio in decibels for each temperature step. It can be concluded that the active vibration controller with parameter adaptation through temperature measurement achieves sufficient peak reductions of around ten decibels and more for all three resonance peaks up to 30°C (86°F). Above this temperature, the performance of the active controller is reduced for the first structural mode due to pole-zero cancellations in the collocated transfer function. Higher-order modes, however, do not experience those cancellations and therefore, sufficient peak reduction is possible for all temperature steps.

Table 5.1. Magnitude Reduction Achieved by Active Controller with Open-Loop Parameter Adaptation through Temperature Measurement.

	Temperature	22.5°C	25°C	30°C	35°C	40°C
First Peak	Magnitude (uncontrolled)	119.4	108.9	53.1	21.7	28.7
	Magnitude (controlled)	28.8	30.0	19.6	17.0	21.7
	Magnitude Reduction	**12.4 dB**	**11.2 dB**	**8.7 dB**	**2.1 dB**	**2.4 dB**
Second Peak	Magnitude (uncontrolled)	78.0	41.8	8.2	19.5	24.5
	Magnitude (controlled)	18.3	12.7	2.8	8.1	11.4
	Magnitude Reduction	**12.6 dB**	**10.3 dB**	**9.3 dB**	**7.6 dB**	**6.6 dB**
Third Peak	Magnitude (uncontrolled)	62.4	46.4	38.1	45.5	36.8
	Magnitude (controlled)	15.5	14.6	11.1	9.5	7.8
	Magnitude Reduction	**12.1 dB**	**10.0 dB**	**10.7 dB**	**13.6 dB**	**13.5 dB**

Concluding this chapter, the experienced drawbacks of the open-loop parameter adaptation with temperature measurement should be mentioned here. First there is the need to measure the collocated transfer function of the actuator-plate-sensor combination for finely graduated temperature steps. This is not only time consuming but it also needs to be repeated for every plate to be controlled, because every plate investigated in this study showed a slightly different temperature behavior. The exact determination of the pole and zero frequencies is especially critical since the performance of the positive position feedback controller depends on those frequencies.

Another problem encountered in this research was that pole and zero frequencies not only depended on the plate temperature but also on the direction how the temperature was reached. In other words, the frequency of the first mode at 30°C (86°F) could be different if the plate was heated up to this temperature than if the plate was cooled down to it. The difference in the frequencies amounted only a few Hertz but enough to affect the controller performance. The next chapter will describe an adaptation method, which does not depend on the measurement of the plate temperature.

Chapter 6

Parameter Adaptation through On-line Pole-Zero Identification

This chapter describes another approach for an active vibration control system using three positive position feedback (PPF) filters in parallel. To counteract the property changes of the test specimen due to temperature variations the parameter of the PPF filters have to be adjusted. In contrast to the previous chapter where an open-loop adaptation algorithm was investigated, this chapter analyzes an on-line pole-zero identification algorithm. From the knowledge of the pole and zero frequencies, the optimal parameters for the PPF filters can be calculated. This chapter also presents the vibration suppression results at different temperatures using the automatically tuned PPF filters.

6.1 Algorithm

As investigated in Chapter 5, the frequencies of the test plates shift significantly when the plates are heated up from room temperature to 40°C (104°F). In fact, the first vibration mode increases its frequency by a factor of over two. The open-loop adaptation from Chapter 5 provided a solution but had several drawbacks. The main problem with the open-loop algorithm was the accuracy of the pre-determined pole and zero frequencies and the different frequency signatures of different plates.

To avoid the problems with non-matching pre-determined and actual properties of the test plate, an on-line pole-zero identification algorithm was developed. The algorithm itself was first introduced by McEver (1999) to identify the frequencies of one pole and one zero. This research extends the capabilities of the algorithm to a theoretical unlimited number of pole-zero pairs. The number of pole-zero pairs, however, needs to be set beforehand.

The pole-zero identification algorithm uses the existing piezoelectric (PZT) actuator to excite the structure and the accelerometer to measure the response. For excitation, a sinusoidal chirp signal is sent through the existing hardware (smoothing filter, Treck power amplifier) to the sensor. Starting with a lower frequency the signal frequency increases as a quadratic function of time up to the ending frequency. The momentary chirp signal frequency can be formulated as

$$f_{chirp}(t) = \left(\frac{f_{end} - f_{start}}{t_{end}^{\ 2}} \right) \cdot t^2 + f_{start} \tag{6.1}$$

where f_{start} and f_{end} are the starting and ending frequencies, respectively, and t_{end} is the total time of the frequency sweep. The quadratic function of time ensures that the sweep remains at lower frequencies long enough to ensure that the number of cycles at lower frequencies is about equal to the number of cycles at higher frequencies. It also allows the transient response to decay [McEver, 1999]. By choosing the starting frequency at 30 Hz and the ending frequency at 400 Hz, all interesting structural poles and zeros were in the range. The Simulink model of the chirp signal generator can be found in Figure C2, Appendix C.

The signal, coming back from the accelerometer on the structure, passes through the PCB Signal Conditioner and undergoes conditioning within the Simulink/dSpace model. At first, a possible DC offset is removed by passing the signal through a first-order high pass filter with the corner frequency set to 0.5 Hz. Then the signal is rectified and sent through a second-order low pass filter with a corner frequency proportional to the bandwidth of the frequency sweep. While Figure 6.1 shows the elements for the signal conditioning symbolically, Figure C3 (Appendix C) presents the actual implementation in Simulink.

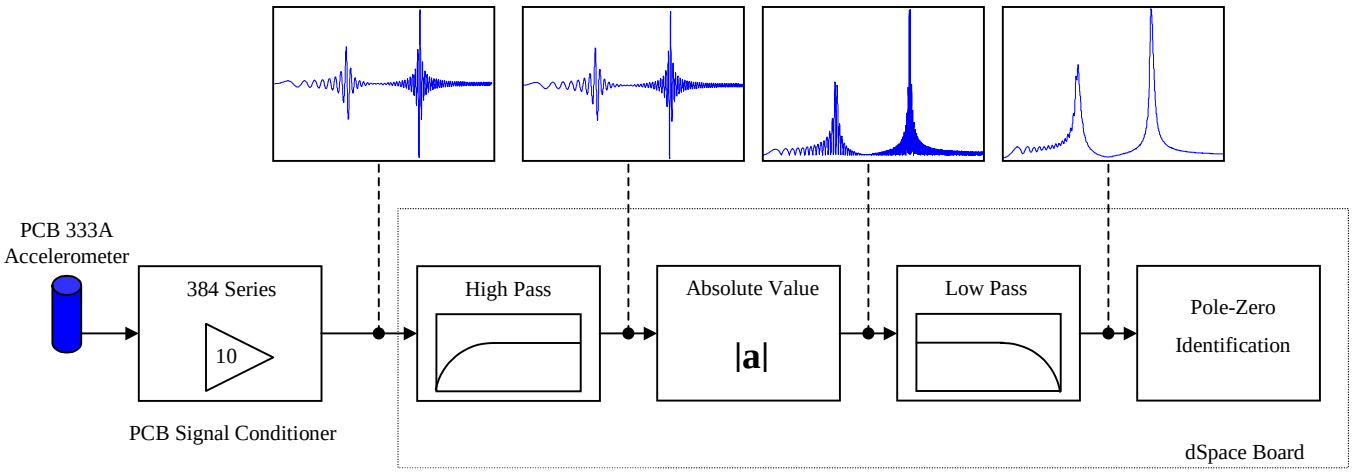

Figure 6.1. Signal Conditioning for the Pole-Zero Identification.

The pole-zero identification algorithm started with a running maximum subsystem and a running minimum subsystem to detect peaks and valleys in the conditioned signal. Because the running maximum and running minimum subsystems had access to the current sine-sweep time, the frequencies of the detected maximums and minimums could be calculated using Equation (6.1). When a maximum in the signal was detected, the running minimum algorithm was reset and enabled for a certain frequency range after the maximum according to

$$\Delta f = 0.1 f_{pole} + 10Hz \tag{6.2}$$

where f_{pole} is the frequency of the detected maximum. The dynamic frequency range was necessary because the poles and zeros of the structure were closer together at lower frequencies than at higher frequencies. After a pole-zero pair was found another subsystem confirmed the validity of the pole frequency and reset the running maximum algorithm. A simple subsystem with logical operators performed this task (Figure C5, Appendix C). If the pole frequency was valid, the parameter subsystem calculated the PPF filter parameters ω_f, ζ_f, and g according to the equations from Section 3.2. Figure 6.2 shows the block diagram of the parameter subsystem in Simulink. Note that one of the inputs in the Simulink block was the gain margin (GM). As the frequency range for the zeros, the gain margin for the parameter calculation was adjusted to 2.5, 5, or 10, depending on whether the parameters were calculated for the first mode, second mode, or third mode, respectively. This ensured best performance for the lower modes, while maintaining stability on the highest mode.

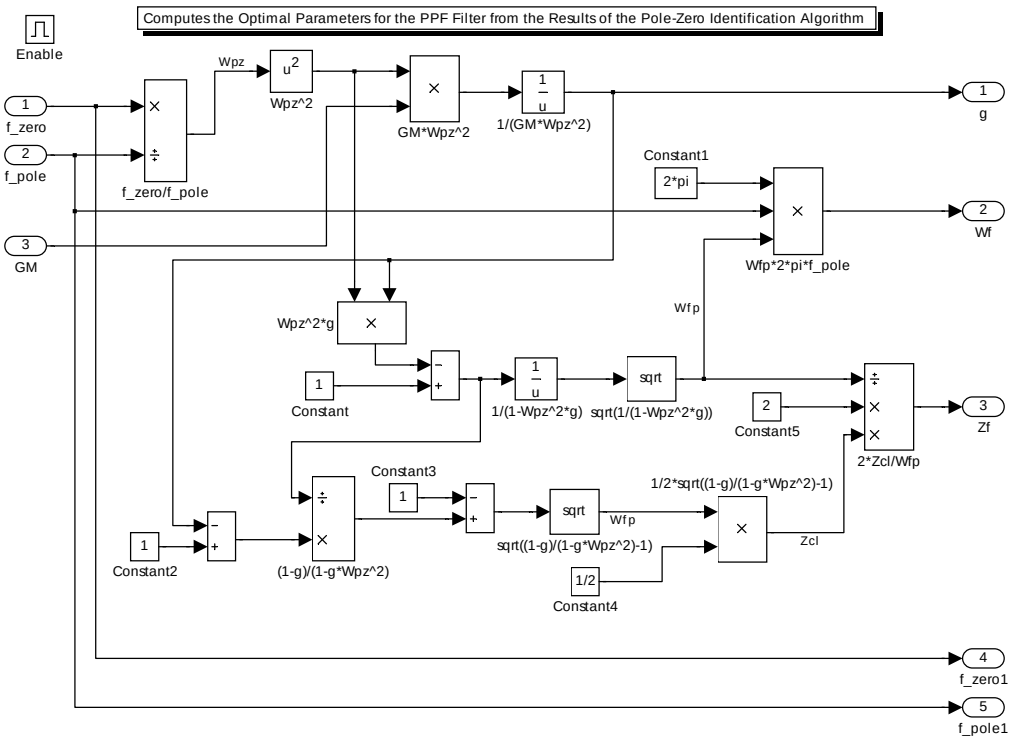

Figure 6.2. Simulink Model for Calculating the Optimal PPF Parameters from the Pole and Zero Frequencies.

To make the parameters available to the PPF filters, each parameter was immediately stored at a data memory location within Simulink/dSpace after it was calculated. When the end of the sine sweep was reached, all pole-zero identification blocks became disabled and the routine switched the three PPF filters on. Figure 6.3 shows the three filters connected to the parameter memories. The figure also shows all the other subsystems in the first level of the Simulink model. Double-clicking on the rectangle in the lower left corner of the Simulink model initialized the sampling time of 0.3 milliseconds and other variables defined in the Matlab script file *"cirp_test_init.m"* (Appendix D). The script file also contained the definitions for the signal conditioning filters and for the pseudo-integrator.

Note that in contrast to the algorithm used by McEver (1999) where two frequency sweeps were performed to identify one pole and one zero, the algorithm developed here only needed one sweep for identifying all pole-zero pairs in the frequency range and therefore, the time until the PPF filters became active, was reduced.

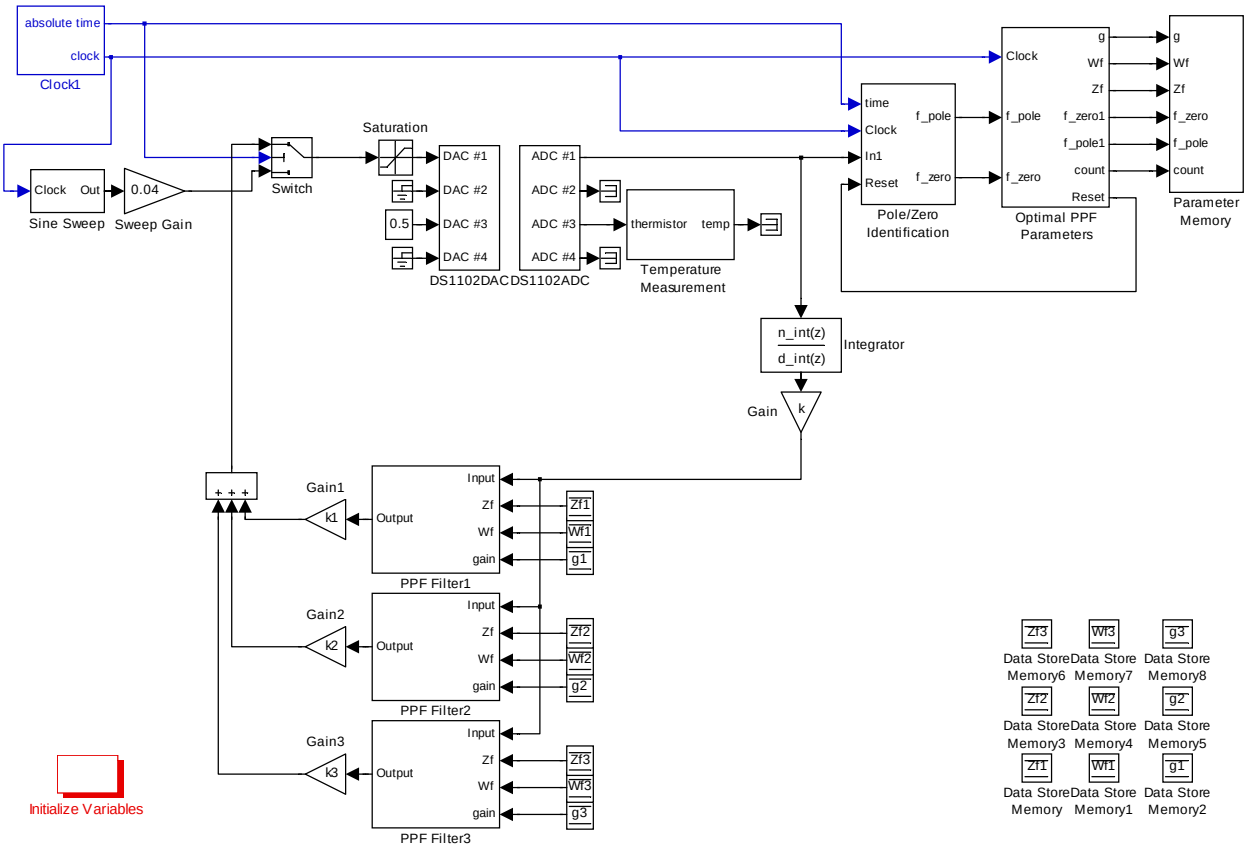

Figure 6.3. Simulink Model for the Active Controller with Three PPF Filters and Parameter Adaptation through On-line Pole-Zero Identification

6.2 Results

This section presents the test results for the active controller with parameter adaptation through the on-line pole-zero identification routine described in Section 6.1. However, before presenting the vibration test results, the performance of the pole-zero identification is analyzed. Over the period of testing, data of the "true" pole and zero frequencies and of the identified pole and zero frequencies were collected. While the true frequencies were measured using the HP signal analyzer as in Figure 4.15, the identified pole and zero frequencies were obtained using the "ControlDesk" software from dSpace.

To analyze the performance of the identification algorithm, the absolute error was computed in Hertz and than normalized by dividing through the true frequency value resulting in the relative error. The mean and the standard deviation of the relative error were calculated separately for each pole and each zero. Table 6.1 presents the calculation results. The numbers in Table 6.1 testify that the pole-zero identification algorithm was able to identify the frequencies correctly. The average overall relative error appeared to be approximately one percent (10.63×10^{-3}). Notice the higher standard deviation values for the zeros, indicating that the identification of the poles was in general more reliable than the identification of the zeros.

Table 6.1. Mean and Standard Deviation of the Relative Identification Error (Values in 10^{-3} Hz/Hz).

$\times10^{-3}$	Pole 1	Zero 1	Pole 2	Zero 2	Pole 3	Zero 3	Overall
Mean	11.04	9.82	6.09	21.61	5.99	6.43	10.63
Standard Deviation	4.76	12.82	3.47	24.49	6.90	5.76	13.64

At this point, a short remark on the notation should be made. As in Chapter 5, the first pole-zero pair refers to the first peak in the frequency response function of the plate at around fifty Hertz. The second pole-zero pair belongs to the third peak in the frequency response, which lies at approximately 150 Hz. And finally, the third pole-zero pair is meant to control the last peak in the frequency response of the plate at around 350 Hz. This distribution of the PPF filter to the resonance peaks ensured best controller performance with the lowest number of PPF filters.

Although the vibration suppression tests were performed without any disturbance on the test specimen during the pole-zero identification, several tests of the pole-zero identification algorithm were run under the presence of disturbances. Using the HP Signal Analyzer to generate multi-frequency vibrations on the plate, the influence on the accuracy of the frequency identification was examined. Two different kinds of disturbances were possible with the HP Signal Analyzer; pink noise and random noise. Whereas the power density of random noise, which is also known as white noise, remains constant over the frequency range, the power density of pink noise decreases about 3 dB per octave (or 10 dB per decade) with increasing frequency. Both noise distributions were applied to the plate at levels from fifty millivolts rms

(root mean square) to three-hundred millivolts rms via the electromagnetic shaker. Note that the level numbers only represent the output voltage of the HP Signal Analyzer but do not describe any acoustic or vibrational noise levels. Table 6.2 presents the mean values of the relative identification errors for all pole and zero frequencies. The numbers indicate that the disturbances do not have significant influence on the accuracy of the frequency identification. The relative error appears to be in the same range as without any disturbance. However, under the influence of pink noise at a level of 300 mVrms the pole-zero pair of the first mode could not be detected at all. The problems with pink noise are due to the higher power density of lower frequencies. It should also be mentioned here that the accuracy of the pole-zero identification also depends on the excitation voltage of the PZT actuator. Throughout this work, a voltage of eight volts peak (5.7 Vrms) was used.

Table 6.2. Mean of the Relative Identification Error for all Pole and Zero Frequencies at the Presence of Disturbances of Different Levels (Values in Hz/Hz).

HP Output Level	50 mVrms	100 mVrms	150 mVrms	200 mVrms	250 mVrms	300 mVrms
Pink Noise	12.05×10^{-3}	4.79×10^{-3}	9.15×10^{-3}	5.02×10^{-3}	10.17×10^{-3}	(8.86×10^{-3})
Random Noise	12.11×10^{-3}	9.37×10^{-3}	8.12×10^{-3}	11.36×10^{-3}	25.94×10^{-3}	16.89×10^{-3}

Knowing that the identification algorithm could detect the pole and zero frequencies very reliably, the vibration suppression tests were started. As in Chapter 5, the test plate was heated up by the infrared lamp in 5°C (9°F) increments. The existing thermistor was used to measure the temperature and to display the value in "ControlDesk." The temperature measurement, however, did not have any influence on the PPF parameter calculation.

After a steady state of the temperature at the desired value was reached, the frequency response function of the uncontrolled plate was taken according to Figure 4.11. Then, the digital signal processor (DSP) was started, causing the pole-zero identification routine to execute and enable the three PPF filters. With the controller switched on, the frequency response of the plate was measured again. Figure 6.4 compares the open-loop and closed-loop plate responses at different temperatures. The achievements of the active control are clearly visible as peak reductions in the frequency response function.

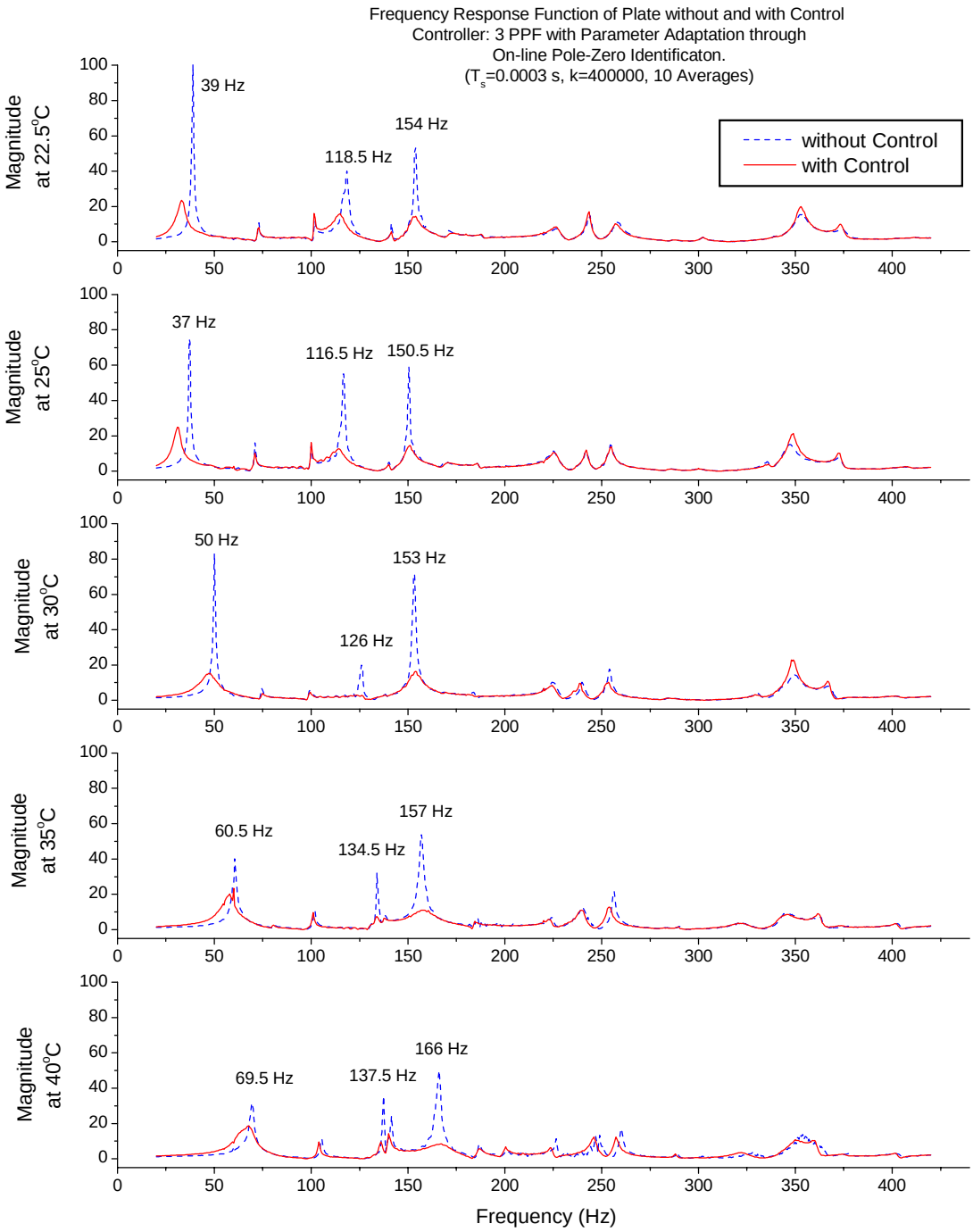

Figure 6.3. Frequency Response Function of Plate without and with Active Control at Different Temperatures.

During the tests, every time another temperature step was reached, the program on the DSP was restarted, hence, executing the pole-zero identification algorithm again. Besides that, no other adjustments were made on the controller. To avoid manual restarts of the controller system, the algorithm could be altered such that the pole-zero identification routine is executed in certain time intervals or when certain performance parameters are reached.

Note that the third PPF filter tuned to the last vibration mode at around 350 Hz did not contribute to a significant magnitude reduction for this mode. The only purpose of the third PPF filter was to minimize possible increases in the magnitude of the higher frequency modes. On the other hand, the second PPF filter was able to decrease the magnitude of two peaks significantly and simultaneously. Table 6.1 summarizes the vibration test results by quantifying the magnitudes of the three largest peaks for the uncontrolled case and for the controlled case. The table also shows the magnitude reduction in decibel achieved with the developed control and adaptation algorithm. The performance loss for the first vibration mode at higher temperatures can be explained with the decrease of the pole-zero spacing ω_{zp}.

Table 6.3. Magnitude Reduction Achieved by Active Controller with Parameter Adaptation through On-line Pole-Zero Identification.

	Temperature	22.5°C	25°C	30°C	35°C	40°C
First Peak	Magnitude (uncontrolled)	100.2	74.9	83.0	40.3	31.6
	Magnitude (controlled)	23.6	24.6.0	15.2	23.4	18.6
	Magnitude Reduction	**12.6 dB**	**9.7 dB**	**14.4 dB**	**4.7 dB**	**4.6 dB**
Second Peak	Magnitude (uncontrolled)	40.2	55.2	20.1	32.2	35.6
	Magnitude (controlled)	15.8	12.6	2.7	7.3	14.2
	Magnitude Reduction	**8.0 dB**	**12.8 dB**	**17.4 dB**	**12.8 dB**	**8.0 dB**
Third Peak	Magnitude (uncontrolled)	53.3	59.0	71.4	54.0	49.8
	Magnitude (controlled)	14.5	14.5	16.3	11.1	8.3
	Magnitude Reduction	**11.3 dB**	**12.2 dB**	**12.8 dB**	**13.7 dB**	**15.6 dB**

This chapter has described the pole-zero identification algorithm for updating the filter parameters of three PPF filter. The algorithm is capable of determining the frequency of a number of pole-zero pairs in the collocated transfer function of a structure even under the presence of noise up to a certain level. The results presented in this chapter show that a controller with three PPF filters tuned to the optimal parameters from Section 3.2 reduced the magnitude of three major resonance peaks in the transfer function of the test specimen significantly. Although the performance of the controller decreased with rising plate temperature due to pole-zero cancellations, the performance of this controller was better than the performance of the controller described in Chapter 5. A drawback of the adaptation process through pole-zero identification was that the adaptation process could not run simultaneously while the PPF filters are in the feedback loop. In other words, during the pole-zero identification process active control is not possible.

Chapter 7

Conclusions

This chapter summarizes the results of this research. In Section 7.1, the vibration suppression results from Chapter 5 and Chapter 6 are compared. Section 7.1 also summarizes the simulation results from Chapter 3. The second part of Chapter 7 discusses unanswered questions from this research leading to recommendations for future research areas.

7.1 Summary

Vibration suppression on flexible structures has been a very important issue especially in the automotive and aircraft industry for reducing acoustic noise levels and minimizing fatigue stress on structures. Active vibration suppression systems using smart material based actuators and sensors are becoming increasingly popular because passive damping materials are limited in their performance and add substantial amounts of weight to the structures. Drawbacks of active control systems include the requirement of adjusting the controller parameters to the structure parameters. If however, the parameters of the structure change over time automatic tuning systems or adaptive control systems become necessary. For instance, aircraft structures are exposed to a wide range of temperatures during a flight. In addition, satellite applications are also subject to continual temperature fluctuations. Since many material constants are temperature dependent, the mechanical properties of structures may change significantly.

This research was conducted on a representative aircraft panel exposed to temperatures between 20°C (68°F) and 40°C (104°F). Over this temperature range the frequency of the first vibration mode of the plate changed from about 40 Hz to over 70 Hz. The frequencies of the other vibration modes also changed, but not so dramatically. The objective of the research was

to increase the structural damping of the first three to four vibration resonance modes using positive position feedback (PPF) filters and smart material based sensors and actuators. The significant shifts in frequencies made the use of fixed parameter PPF filters impossible. This thesis has represented two approaches to encounter the frequency shifts of the plate. First, an open-loop adaptation algorithm was investigated in Chapter 5. The algorithm utilized a temperature sensor on the plate and pre-determined information about the pole and zero frequencies of the plate at 2.5°C (4.5°F) temperature increments. Using the results from Section 3.2, the optimal PPF parameters were calculated for each temperature increment. Implemented through Simulink/dSpace the parameters of the three PPF filters were constantly updated according to the current plate temperature. Sufficient magnitude reductions as high as 13.6 dB for the third vibration mode were achieved using the open-loop adaptation algorithm. For the first vibration mode however, the performance of the controller was insufficient at higher temperatures. This was mainly due to pole/zero cancellation effects but also due to inaccuracies in the pre-determined pole and zero frequencies.

To overcome the disadvantages of the open-loop adaptation algorithm an auto-tuning method was investigated in Chapter 6. Using a sinusoidal chirp signal with the frequency increasing as a quadratic function of time, the pole and zero frequencies of the test structure were determined online. Then, the algorithm computed the optimal parameters for the three PPF filters. After updating the parameters, the controller was activated and achieved magnitude reductions up to 17.4 decibel. Although the auto-tuned controller did not reach those high reduction levels for every temperature and vibration mode, on the average its performance was better than the performance of the open-loop adaptation controller. Figure 7.1 compares the reduction levels of both controllers for the first three vibration peaks over the temperature range of interest.

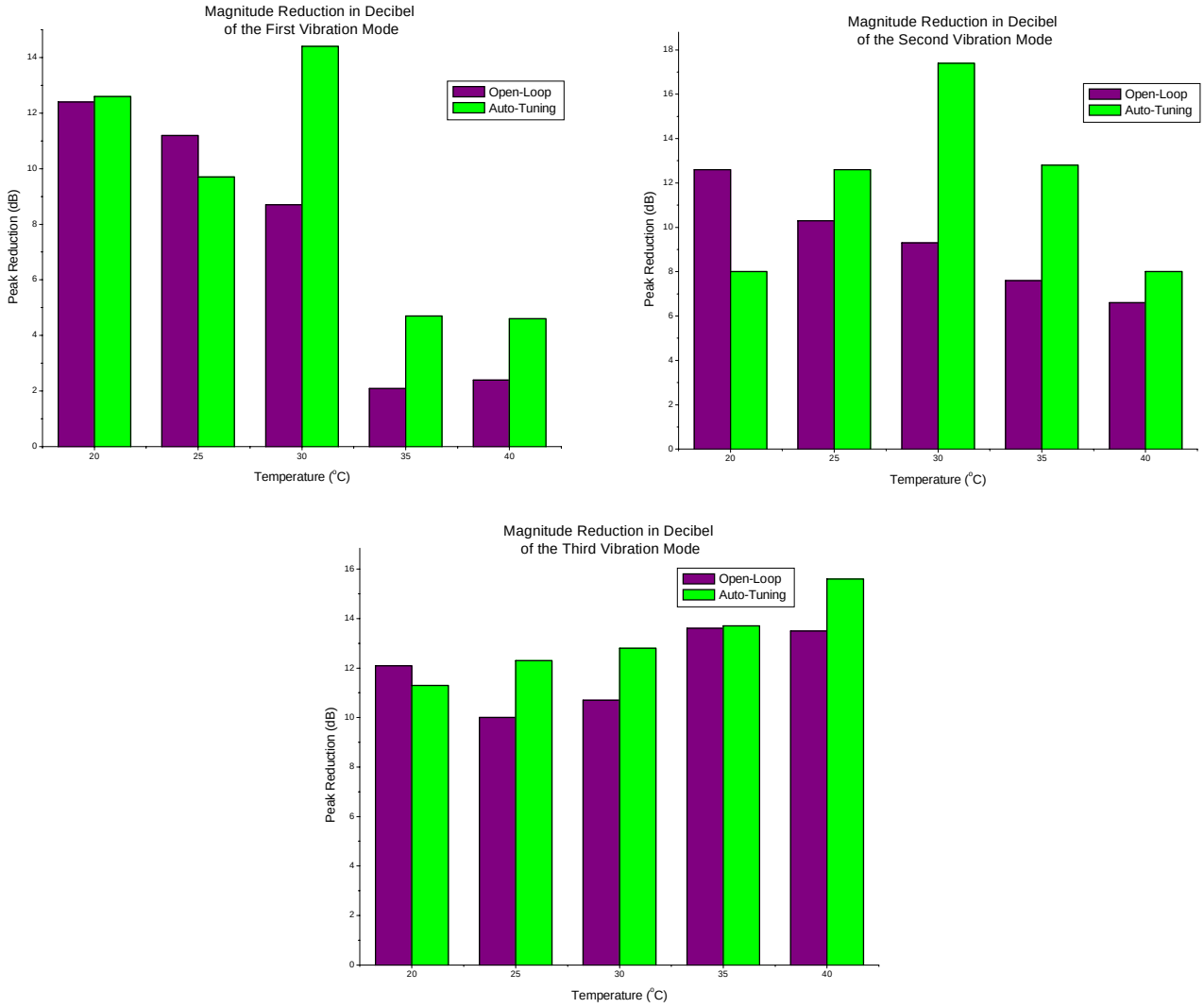

Figure 7.1. Magnitude Reductions of the Open-Loop Adaptation Controller and the Auto-Tuned Controller.

Other results of this research were provided by the simulations in Section 3.3. The simulations of digital PPF filters showed that the fastest possible sampling rate might result in lower controller performance than a sampling rate chosen 4 to 14 times higher than the pole frequency of the structure to be damped. Furthermore, Section 3.3 presented interesting effects of the zero-order hold (ZOH) digitization on the collocated transfer function of the plant. While the structural pole is transformed correctly in the digital domain, the zero of the continuous time transfer function does not appear at all in the frequency response of the transformed plant for a sampling rate 5 times as high as the zero frequency. Sampling rates as high as 130 times of zero

frequency are needed to match the frequency response of the sampled plant to the response of the original, continuous time plant.

In conclusion, it can be said that the objectives of this research were fulfilled. An accelerometer was selected as the vibration sensor and a piezoelectric ceramic patch worked as the actuator over the temperature range of interest. Using three PPF filters, the damping of the three lowest vibration resonance modes was increased significantly. An automatic tuning algorithm for the PPF filters was developed in Chapter 6. Chapter 6 also showed that the auto-tuning algorithm detects the poles and zeros of the structure within an average error of about one percent. Under the presence of external disturbances up to a certain level, this identification error did not increase. Exceeding that disturbance level caused the identification routing not to be able to find the structural poles and zeros at all. The next section will present questions and problems encountered during this research, which could lead to future studies in this research area.

7.2 Future Work

The research conducted for this thesis has shown a great potential for future work in the area of smart material techniques and digital, structural control. Particularly, the determination of the optimal parameters for digital positive position feedback (PPF) filters is of great interest. The effects of the sampling rate and of the transformation method also need further investigation.

To encounter thermally induced changes in the structure, this research has presented an open-loop adaptation method and an auto-tuning method for adjusting the parameters of PPF filters. The development of a “real” adaptive system using a closed-loop adaptation process would lead to a more universal controller. The controller should update itself in real time making the offline measurements and the identification routine superfluous. Other adaptation laws based on LMS techniques, neural networks, or genetic algorithms are also possible.

Another very interesting area is the research on the thermal effects of the structure. The author has not found any literature on the observed effect that the resonance frequencies of a heated plate shift by a factor of more than two, compared to the unheated plate. The same study

could include investigations on the optimal sensor/actuator location. Finite element models could explain why a PZT-sensor/PZT-actuator system results in very closely spaced poles and zeros which lead to pole/zero cancellations while an accelerometer/PZT-actuator systems has much wider spaced poles and zeros. Why does the pole/zero spacing change at all when the test specimen is heated up is also an interesting question.

Although this research has concentrated on PPF filters for vibration suppression, it does not mean that PPF is the best control law for those tasks. Other control laws might be better suited, especially if closed-loop adaptation methods are to be implemented. The control effort (power to drive the actuators) is an important issue for automotive, aircraft, and satellite application, since higher control efforts require more energy and heavier amplifiers. Different control laws might achieve vibration reductions but with different control efforts. Therefore, a study investigating and comparing the control effort of different control laws is very valuable.

Last but not least, there is still some effort necessary to make piezoelectric actuators more reliable. During the weeks of the experiments for this research, three actuators broke in spite of the precautions taken. The testing conditions might have been somewhat extreme due to the thermally induced mechanical stress but “real” automotive, aircraft, and satellite applications may come close to these conditions.

References

Agnes, G. S., *Performance of Nonlinear Mechanical, Resonant-Shunted Piezoelectric, and Electronic Vibration Absorbers for Multi-Degree-of-Freedom Structures,* Dissertation (Blacksburg: Virginia Tech, 1997).

Aldrich, J.B., Hagood, N.W., von Flotow, A, and Vos, D.W., "Design of Passive Piezoelectric Damping for Space Structures," *Proceedings of the SPIE-The International Society for Optical Engineerin*g, Vol. 1917, No. 2 (1993), pp. 692-705.

Åström, K. J., Wittenmark, B., *Adaptive Control,* First Edition (Reading: Addison-Wesley Publishing Company, 1989).

Bay, J. S., *Fundamentals of Linear State Space Systems,* First Edition (Boston: McGraw-Hill, 1999).

Baz, A., Hong, T. H., "Adaptive Control of Flexible Structures Using Modal Positive Position Feedback," *International Journal of Adaptive Control and Signal Processing,* Vol. 11 (1997), pp. 231-253.

Baz, A., Poh, S, "Optimal Vibration Control with Modal Positive Position Feedback," *International Journal of Optimal Control Applications & Methods,* Vol. 17 (1996), pp. 141-149.

Baz, A., Poh, S., Fedor J., "Independent Modal Space Control with Positive Position Feedback," *Journal of Dynamic Systems, Measurement and Control (Transactions of the ASME),* Vol. 114 (1992), pp. 96-103.

Caughey, T. K., Goh, C. J., "Analysis and Control of Quasi-Distributed Parameter Systems," *Dynamics Laboratory Report* DYNL-82-3 (1982), California Institute of Technology, Pasadena.

DeGuilio, A. P., *A Comprehensive Experimental Evaluation of Actively Controlled Piezoceramics with Positive Position Feedback for Structural Damping*, Master Thesis (Blacksburg: Virginia Tech, 2000).

Dosch, J. J, Leo, D., Inman, D. J., "Modeling and Control for Vibration Suppression of a Flexible Active Structure," *Journal of Guidance, Control, and Dynamics*, Vol. 18 No. 2 (1995).

Dosch, J. J., Calamita, J. P., Inman, D. J., "Performance of a Programmable Structure," , *SPIE Conference on Mathematics and Control in Smart Structures*, Vol. 1919 (1993), pp. 151-156.

Dosch, J. J., Inman, D. J., Garcia, E., "A Self-Sensing Piezoelectric Actuator for Collocated Control," *Journal of Intelligent Material Systems and Structures*, Vol. 3 (1992).

Fagan, G. T., *An Experimental Investigation into Active Damage Control Systems Using Positive Position Feedback for AVC*, Master Thesis (Blacksburg: Virginia Tech, 1993).

Fanson, J. L., Cauhey, T. K.," Positive Position Feedback Control for Large Space Structures," *AIAA Journal*, Vol. 28, No. 4 (1990), pp. 717-724.

Fanson, J. L., Chen, J. C., "Structural Control by the Use of Piezoelectric Active Members," *NASA-Conference-Publication*, 2447, pt 2 (1986), pp. 809-829.

Forward, R. L., "Electronic Damping of Vibrations in Optical Structures," *Applied Optic*s, Vol. 18, No. 5 (1979), pp. 690-697.

Franklin, G. F., Powell, J. D., Workman M., *Digital Control of Dynamic Systems*, Third Edition (Menlo Park: Addison-Wesley, 1998).

Friedland, B., *Control System Design*, First Edition (Boston: McGraw-Hill, 1986).

Friswell, M. I., Inman, D. J., “The relationship between Positive Position Feedback and Output Feedback Controllers,” *Journal of Smart Materials and Structures*, Vol. 8 (1999), pp. 285-291.

Friswell, M. I., Inman, D. J., Rietz, R. W., “Active Damping of Thermally Induced Vibrations,” *Journal of Intelligent Material Systems and Structures*, Vol. 8 (1997), pp. 678-685.

Goh, C. J., Caughey, T. K., “On the Stability problem Caused by Finite Actuator Dynamics in the Collocated Control of Large Space Structures,” *International Journal of Control*, Vol. 41, No. 3 (1985), pp. 787-802.

Goh, C. J., Lee, T. H., “Adaptive Modal Parameters Identification for Collocated Position Feedback Vibration Control,” *International Journal of Control*, Vol. 53, No. 3 (1991), pp. 597-617.

Hagood, N. W. and von Flotow, A., “Damping of Structural Vibrations with Piezoelectric Materials and Passive Electrical Networks,” *Journal of Sound and Vibration*, Vol. 146, No. 2 (1991), pp.243-268.

Hevey, S. J., *Adaptive Control Using IIR Lattice Filters*, Master Thesis (Blacksburg: Virginia Tech, 1998).

Inman, D. J., *Engineering Vibration*, First Edition (Englewood Cliffs: Prentice Hall, 1996).

Inman, D. J., Hegewald, T., “Suppressing Plate Vibrations with Smart Materials,” *Seventh International Congress on Sound and Vibration* (2000).

Jeric, K. M., *An Experimental Evaluation of the Application of Smart Damping Materials for Reducing Structural Noise and Vibrations*, Master Thesis (Blacksburg: Virginia Tech, 1999).

Kim, Lee, Moon, “Active Suppresion of Plate Vibration with Piezoceramic Actuator/Sensor Using Multiple Adaptive Feedforward with Feedback Loop Control Algorithm,” *SPIE Conference on Mathematics and Control in Smart Structures*, Vol. 3667 (1999).

Kreisselmeier, G., “An Approach to Stable Adaptive Control,” *Automatica*, Vol. 21, pp. 425-431.

Kreisselmeier, G., Narendra, K. S., “Stable Model Reference Adaptive Control in the Presence of Bounded Disturbances,” *IEEE Transaction on Automatic Control*, Vol. 27, pp. 1169-1175.

Kwak, M. K., Denoyer, K., “Tuning of Active Vibration Controllers for ACTEX by Genetic Algorithm,” *SPIE Conference on Smart Structures and Integrated Systems*, Vol. 3668 (1999).

Kwak, M. K., Han, S. B., “Application of Genetic Algorithm to the Determination of Multiple Positive Position Feedback Controller Gains for Smart Structures,” *SPIE Conference on Mathematics and Control in Smart Structures,* Vol. 3323 (1998).

Kwak, M. K., Shin, T. S., “Real-Time Automatic Tuning of Vibration Controllers for Smart Structures by Genetic Algorithm,” *SPIE Conference on Mathematics and Control in Smart Structures*, Vol. 3667 (1999).

Leo, D. J., Inman, D. J., “Pointing Control and Vibration Suppression of a Slewing Flexible Frame,” *Journal of Guidance, Control, and Dynamics,* Vol. 17, No. 3 (1994), pp. 528-536.

McEver, M. A., *Optimal Vibration Suppression Using On-line Pole/Zero Identification,* Master Thesis (Blacksburg: Virginia Tech, 1999).

Poh, S., Baz, A., “Active Control of a Flexible Structure Using a Modal Positive Position Feedback Controller,” *Journal of Intelligent Material Systems and Structures,* Vol. 1 (1990), pp. 273-288.

Scruggs, J., *Active, Regenerative Control of Civil Structures,* Master Thesis (Blacksburg: Virginia Tech, 1999).

Song, G., Schmidt, S. P., Agrawal, B. N., "Experimental Study of Active Vibration Suppression of a Flexible Structure Using Smart Material and Modular Control Patch," *IEEE Aerospace Applications Conference Proceedings,* Vol. 1 (1998), pp. 189-201.

Sprangler, R. L., Russo, F. M., Palombo, D. A., "A Compact, Integrated Piezoelectric Vibration Control Package," *SPIE Proceedings,* Vol. 3041 (1997).

Physik Instrumente (1), "Definition of Piezoelectric Coefficients and Directions," *http://www.physikinstrumente.com/tutorial/4_16.html* (Waldbronn, Germany: Physik Instrumente (PI) GmbH & Co., 1999).

Physik Instrumente (2), "PI Product Line," *http://www.physikinstrumente.com/products.html* (Waldbronn, Germany: Physik Instrumente (PI) GmbH & Co., 1999).

Piezo Systems (1), "Piezo Systems Product Catalog," *http://www.piezo.com/catalog.html* (Cambridge: Piezo Systems Inc.).

Piezo Systems (2), "Piezoelectric Single Sheet, 5H Ceramic," *http://www.piezo.com/sshs4.html* (Cambridge: Piezo Systems Inc.).

SensorTech, "Definition & Terms," *http://www.sensortech.ca/definitions.html* and *http://www.sensortech.ca/fig1-3.html* (Collingwood, Canada: Sensor Technology Ltd., 1999).

Appendix A. Finite Element Model of Plate.

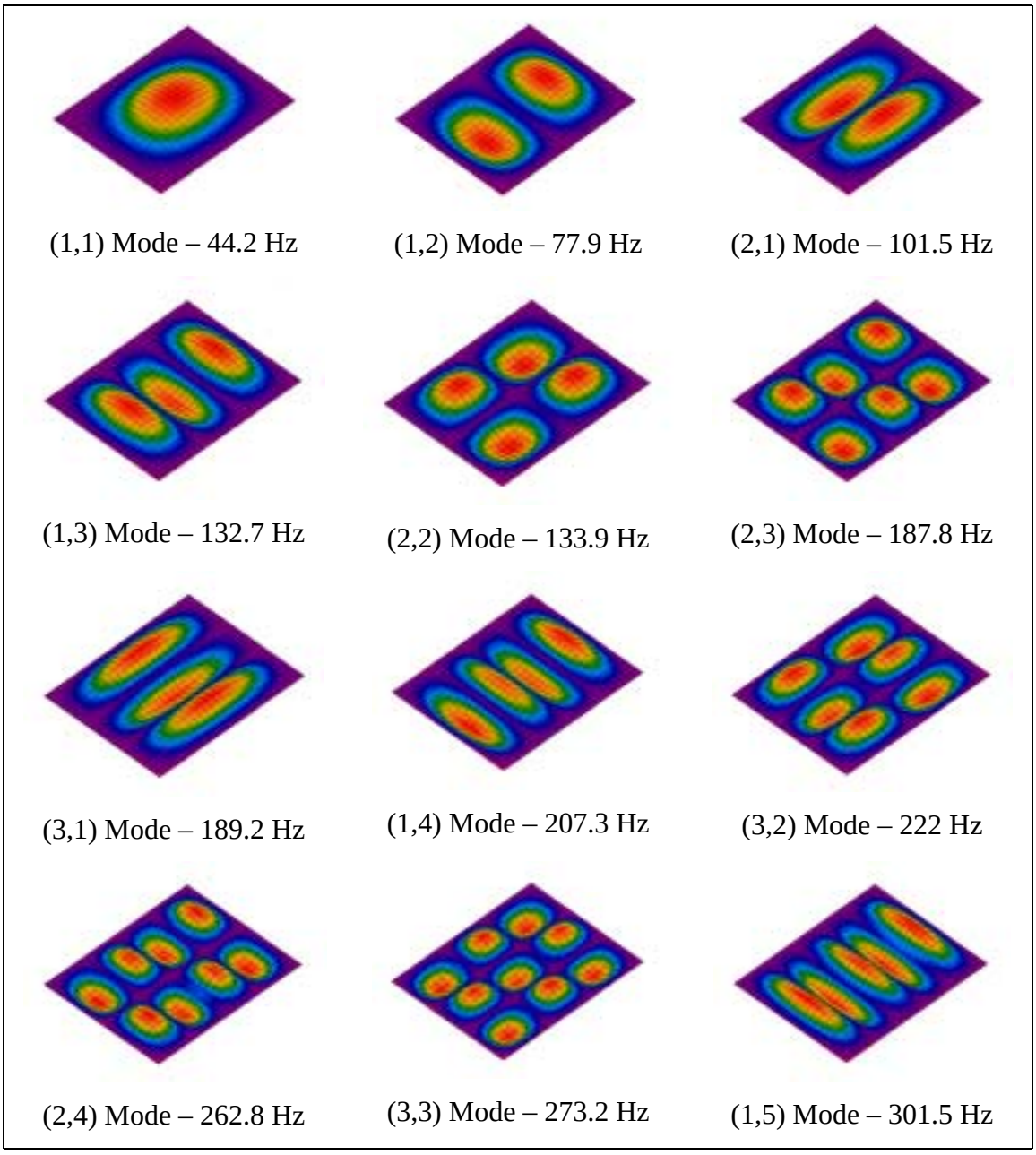

Figure A1. Finite Element Model Results of Test Plate [DeGuilio, 2000]

Appendix B. Collocated Transfer Function

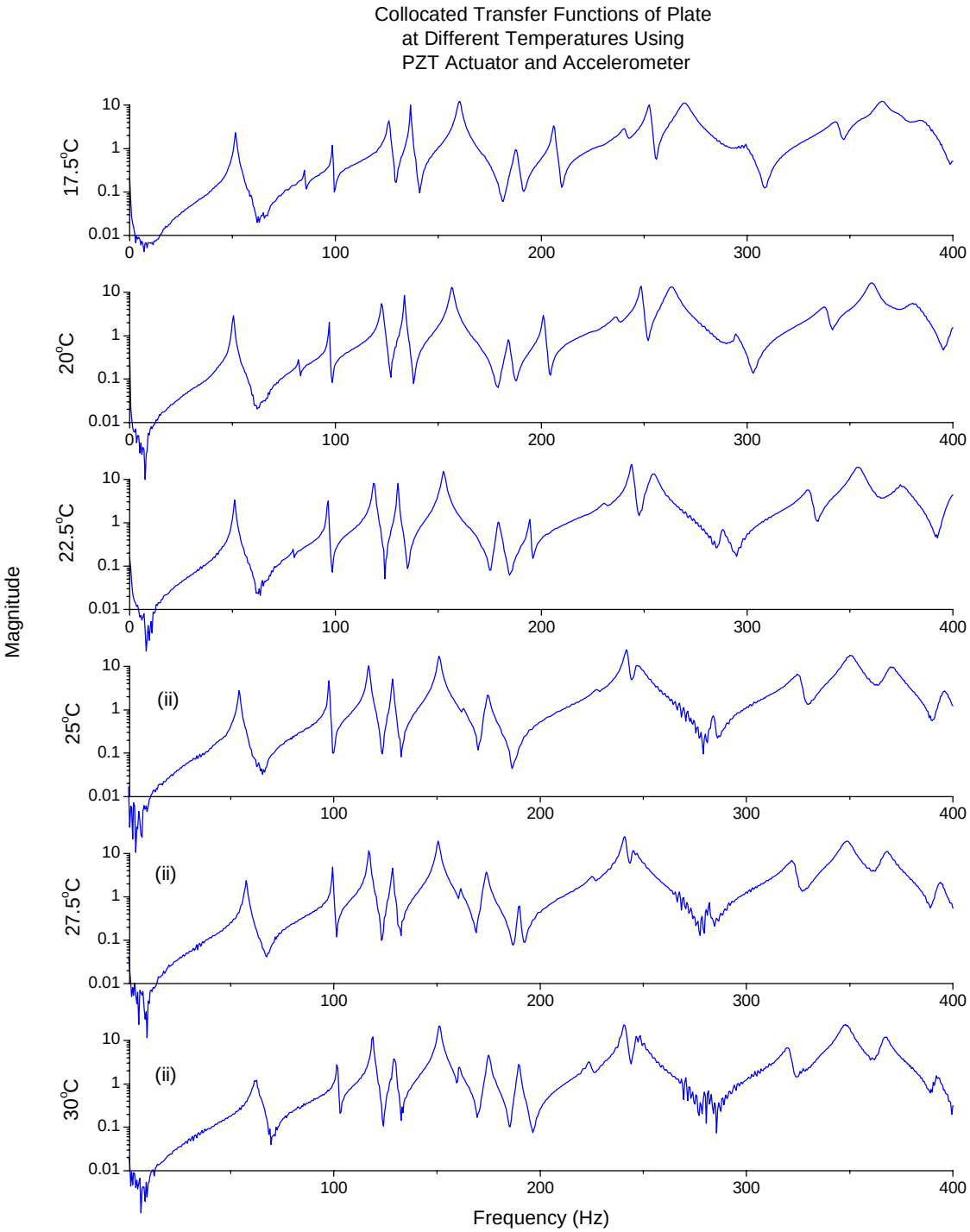

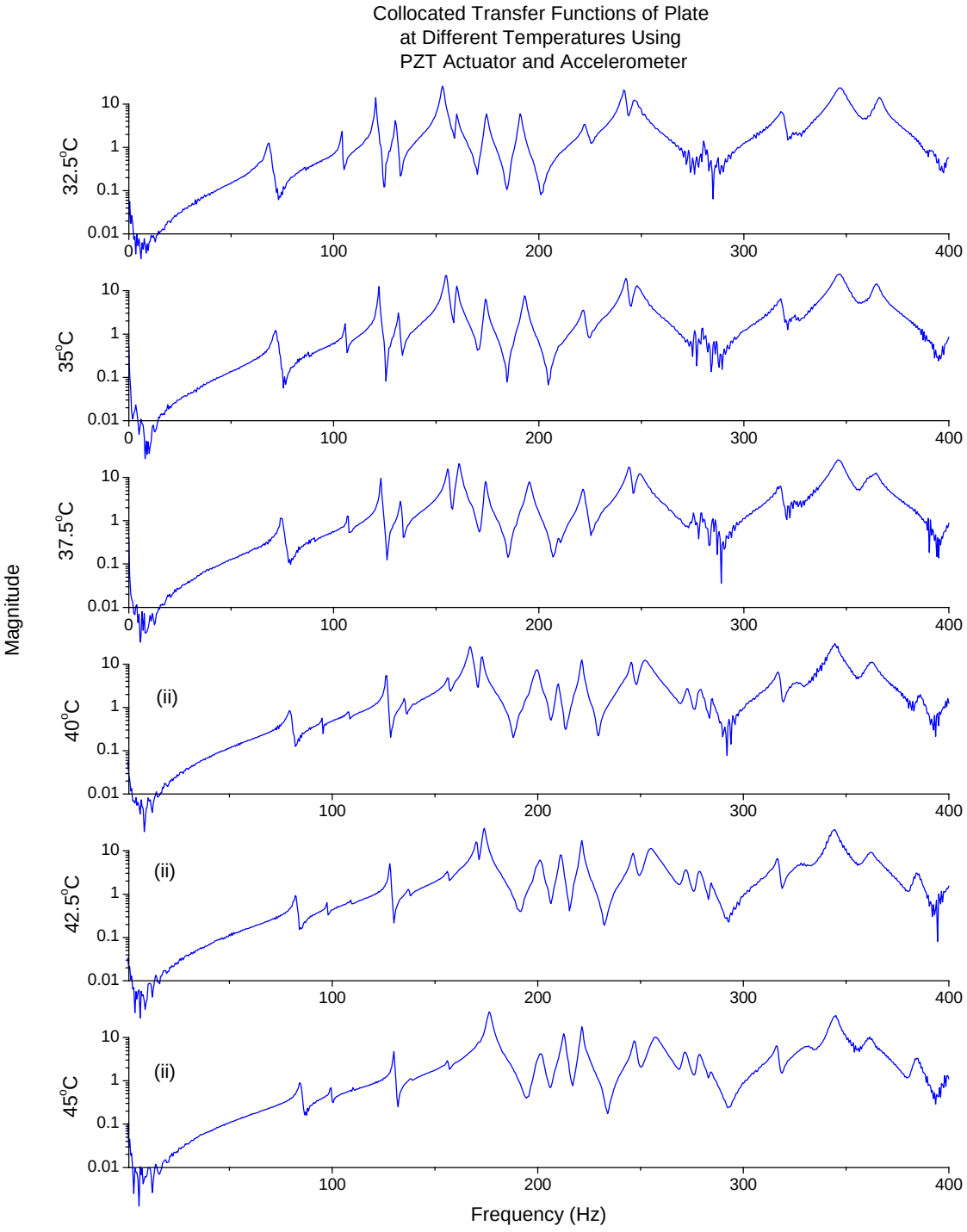

Figure B1. Collocated Transfer Function between PZT Actuator and Accelerometer at Temperatures from 17.5°C (63.5°F) to 45°C (113°F).

Appendix C. Simulink Models

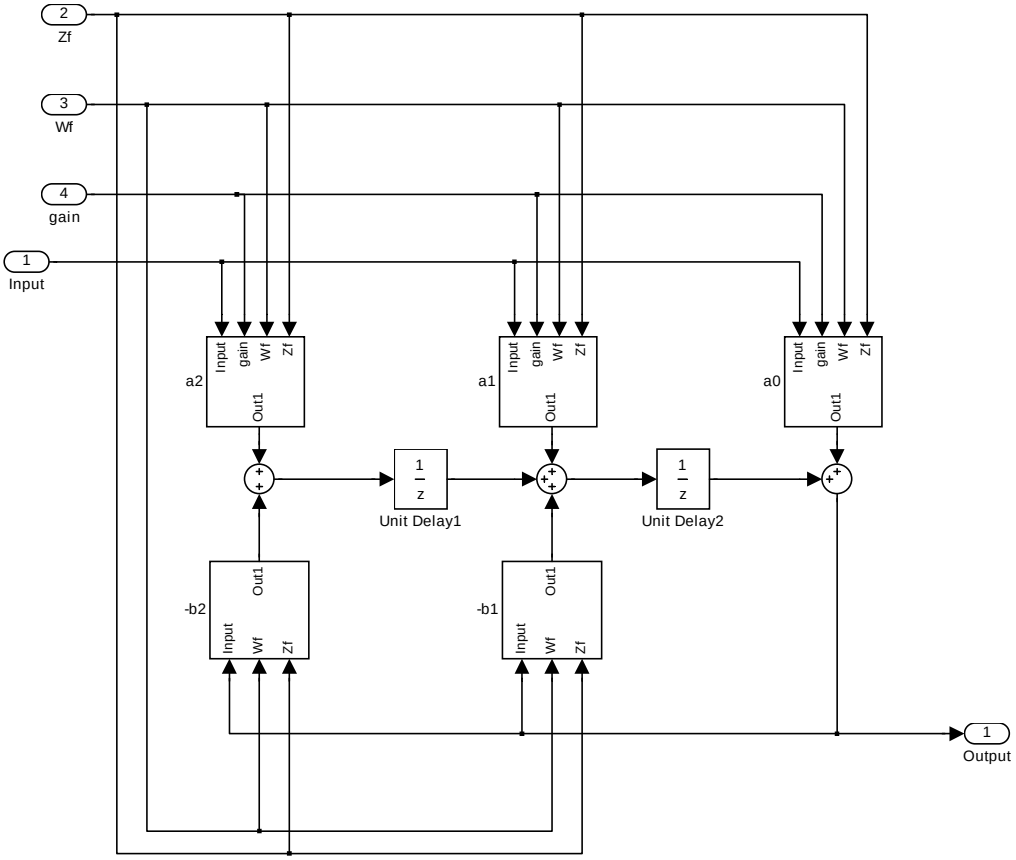

Figure C1. Simulink Model of the Digital PPF Filter.

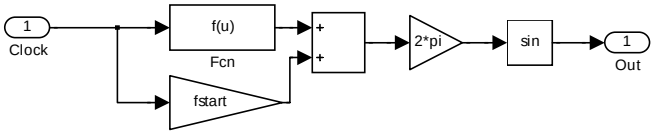

Figure C2. Simulink Model of the Chirp Signal Generator.

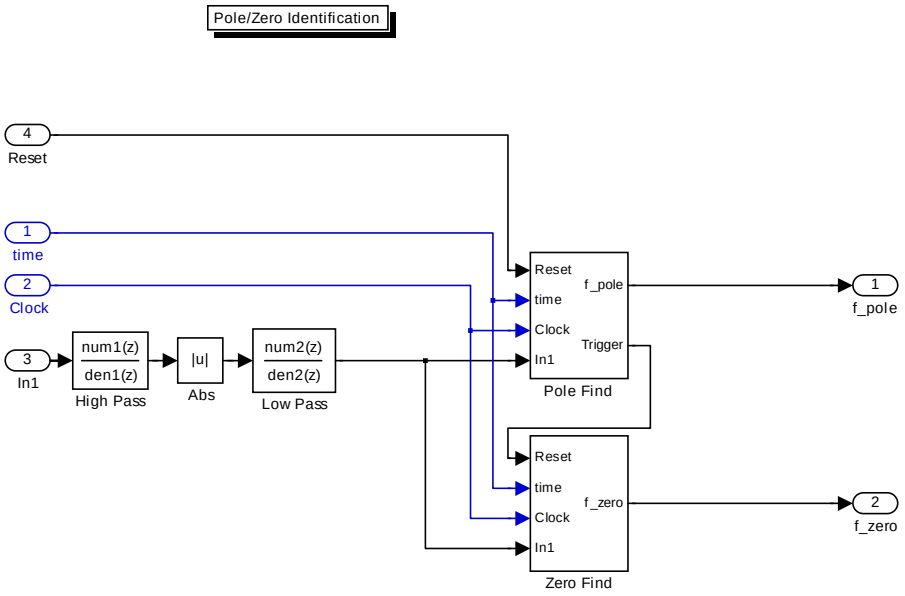

Figure C3. Simulink Model of the Pole/Zero Identification Routine.

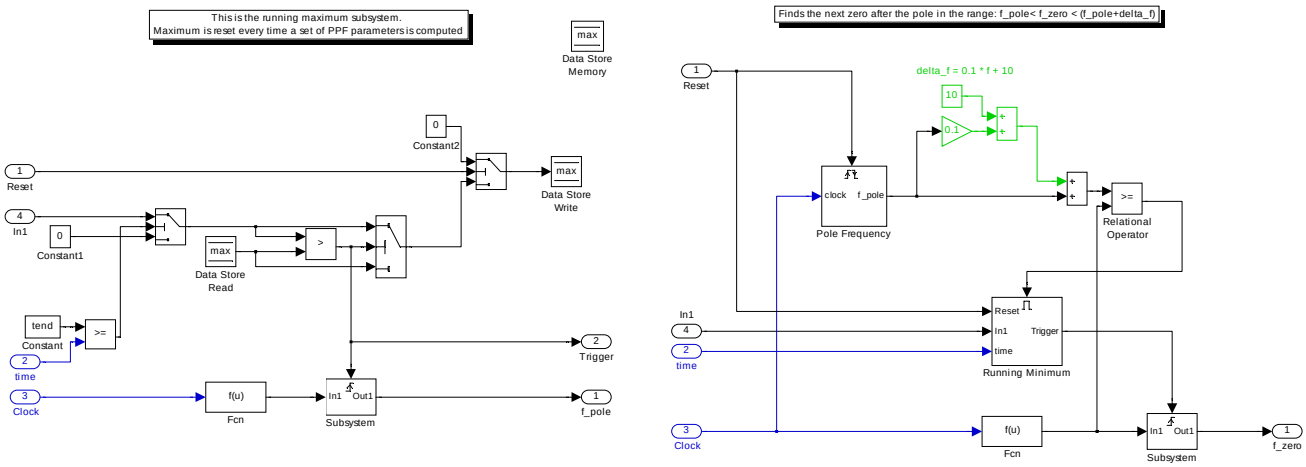

Figure C4. Pole-Find (left) and Zero-Find (right) Subroutines.

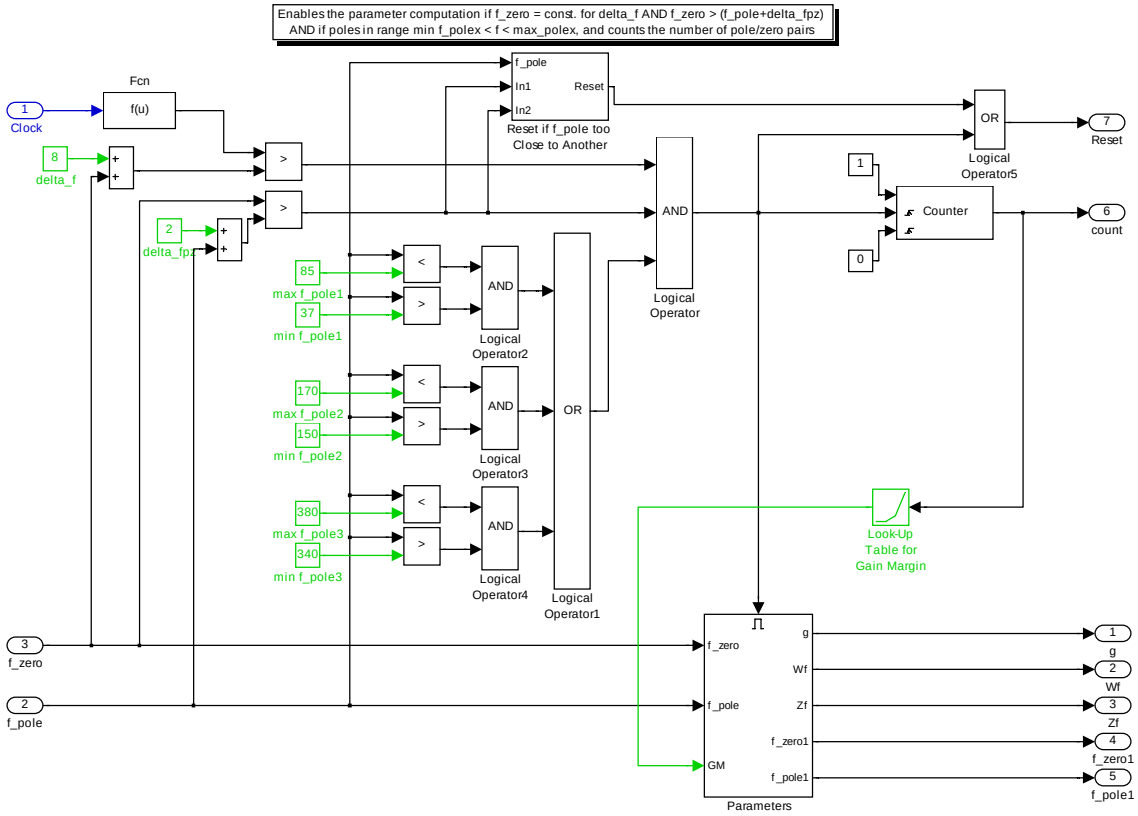

Figure C5. Simulink Subsystem for Enabling the Parameter Calculation.

Appendix D. Matlab Files

File D1. "lookup.m"

```
%creates look-up table for ppf parameters
%Thomas Hegewald
%04/11/00

clear all

temp=[19.5 20 22.5 25 27.5 30 32.5 35 37.5 40 42.5 45 47.5 50];    %temperature steps

%pole and zero frequencies at the certain temperature steps
pole1=[53 53.5 57.5 62 68 72 75.5 79 82 84 87.5 90.5 94 99];
zero1=[64 62.5 66 68.5 71.5 74.5 77 80 83 86.5 89.5 92.5 96.5 101];
pole2=[153 152 151.5 154.5 155.5 166 171 181.5 185.5 192 194 196 201.5 207.5];
zero2=[178.5 177 177 192 196 201 205 210 216.5 219 219 220 220 222];
pole3=[268 266.5 263.5 264 265 270 274 277 280 282 285 290 295 300];
zero3=[303 300 297.5 294.5 293.5 293.5 293.5 294.5 296 298 300 305 310 315];

Wpz1=zero1./pole1;
Wpz2=zero2./pole2;
Wpz3=zero3./pole3;

%optimal PPF parameter

GM=5;                                %Gain margin

g1=1./GM./Wpz1.^2;               % gain
g2=1./GM./Wpz2.^2;
g3=1./GM./Wpz3.^2;

Wfp1=sqrt(1./(1-g1.*Wpz1.^2));    % relative frequency
Wfp2=sqrt(1./(1-g2.*Wpz2.^2));
Wfp3=sqrt(1./(1-g3.*Wpz3.^2));

Wf1=Wfp1.*pole1.*2.*pi;              % filter frequency
Wf2=Wfp2.*pole2.*2.*pi;
Wf3=Wfp3.*pole3.*2.*pi;
```

```
Zcl1=1/4.*sqrt((1-g1)./(1-g1.*Wpz1.^2)-1);  % close-loop damping ratio
Zcl2=1/4.*sqrt((1-g2)./(1-g2.*Wpz2.^2)-1);
Zcl3=1/4.*sqrt((1-g3)./(1-g3.*Wpz3.^2)-1);

Zf1=2.*Zcl1./Wfp1;               %  filter damping ratio
Zf2=2.*Zcl2./Wfp2;
Zf3=2.*Zcl3./Wfp3;

save ppf_parameters g* Wf* Zf* temp;

clear all;
```

File D2. "adapt_init.m"

```
%Adapt_init.m
%initializes the Simulink model
%April 11, 2000, Thomas Hegewald

clear all;

T=0.00025;     %sampling time

%integrator
int_c=tf([1 0],conv(conv([1 2*pi*4.5],[1 2*pi*4.5]),[1 2*pi*4.5]));
int_d=c2d(int_c,T,'foh');
[n_int,d_int]=tfdata(int_d,'v');
n_int=1*n_int;

load ppf_parameters;      %load parameters for look-up table

k1=0; k2=0; k3=0;
k=500000;
```

File D3. "chirp_test_init.m"

```
%Chirp_test_init.m
%initializes the Simulink model
%May 3, 2000, Thomas Hegewald
```

```
clear all;

T=0.0003;      %sampling time


%sine sweep
tend=40;           %time for the chirp signal
fend=400;      %end frequency in Hz
fstart=30;     %start frequency in Hz


%pre-filter
pre_f_c=tf([1 0],[1 2*pi*0.5]);
pre_f_d=c2d(pre_f_c,T,'tustin');
[num1,den1]=tfdata(pre_f_d,'v');

%lowpass filter for pole/zero routine
lowpassc        =        tf([4*pi^2*((fstart+fend)/2)^2],conv([1        2*pi*(fstart+fend)/2],[1
2*pi*(fstart+fend)/2]));
lowpassd = c2d(lowpassc,T,'tustin');
[num2,den2] = tfdata(lowpassd,'v');


%integrator
int_c=tf([1 0],conv(conv([1 2*pi*4.5],[1 2*pi*4.5]),[1 2*pi*4.5]));
int_d=c2d(int_c,T,'foh');
[n_int,d_int]=tfdata(int_d,'v');

k=0;  %400000;     %integrator gain
k1=1;
k2=1;
k3=1;
```

Appendix E. PZT Actuator and Accelerometer Data

PIEZOELECTRIC SINGLE SHEET 5H Ceramic H4E Series

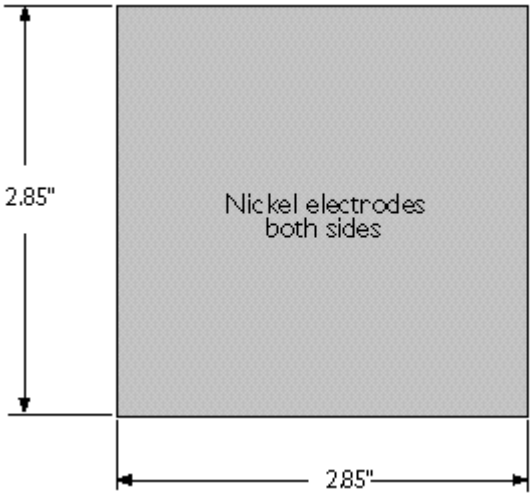

Figure E1. PZT Dimensions [Piezo Systems (2)].

Table E1. Thickness and Capacitance Specifications of PZT.

Part Number	Thickness		Capacitance
	mm	inch	nF (±10%)
T105-H4E-602	0.127	0.005	1250
T107-H4E-602	0.191	0.0075	850
T110-H4E-602	0.267	0.0105	610

Table E2. Piezoelectric, Mechanical, and Thermal Properties of PZT.

PIEZOELECTRIC		
Composition		Lead Zirconate Titanate
Material Designation		PSI-5H-S4-ENH
Relative Dielectric Constant (@ 1 KHz)	K^T_{33}	3800
Piezoelectric Strain Coefficient	d_{33}	650 x 10^{-12}Meters/Volt
	d_{31}	-320 x 10^{-12}Meters/Volt
Piezoelectric Voltage Coefficient	g_{33}	19.0 x 10^{-3}Volt Meters/Newton
	g_{31}	-9.5 x 10^{-3}Volt Meters/Newton
Coupling Coefficient	k_{33}	0.75
	k_{31}	0.44
Polarization Field	E_p	1.5 x 10^6Volts/Meter
Initial Depolarization Field	E_c	3.0 x 10^{-5}Volts/Meter
MECHANICAL		
Density		7800Kg/Meter^3
Mechanical	Q	30
Elastic Modulus	Y^E_3	5.0 x 10^{10}Newtons/Meter^2
	Y^E_1	6.2 x 10^{10}Newtons/Meter^2
THERMAL		
Thermal Expansion Coefficient		~3 x 10^{-6}Meters/Meter °C
Curie Temperature		250°C

PZTs available from:

PIEZO SYSTEMS, INC.

Cambridge, Massachusetts, U.S.A.

Tel: 617-547-1777 Fax: 617-354-2200

http://www.piezo.com

MODEL 333A MODAL ARRAY ACCELEROMETER, 100 mV/g

Table E3. Model 333A, Shear ICP® Accelerometer Data

Voltage Sensitivity (±20%)	100 mV/g (10.2 mV/[m/s^2])
Measurement Range (for ±5 V output)	±50 g pk (±491 m/s^2 pk)
Frequency Range (±5%)	1 to 1 000 Hz
Mounted Resonant Frequency	> 5 kHz
Broadband Noise (1 Hz to 10 kHz)	0.0006 g rms (0.006 m/s^2 pk)
Operating Temperature Range	0 to +150 °F (-18 to +66 °C)
Sensing Element	Ceramic Shear
Size (diameter x height)	0.42 x 0.86 inch (10.7 x 21.8 mm)
Weight	0.15 oz (4 g)
Electrical Connector	3-Pin Socket

Accelerometer available from:

PCB Piezotronics

3425 Walden Avenue, Depew, New York 14043 USA

http://www.pcb.com

PRECISION THERMISTOR 10kΩ (±1%)

Fifth-Order Polynomial for Simulink Model:

$$T = 94.86972 - 14.67769*R_1 + 0.17105*R_1^2 - 0.05065*R_1^3 + 0.00107*R_1^4 - 8.60799e\text{-}6*R_1^5$$

where T is the current temperature and R_1 is the thermistor resistance.

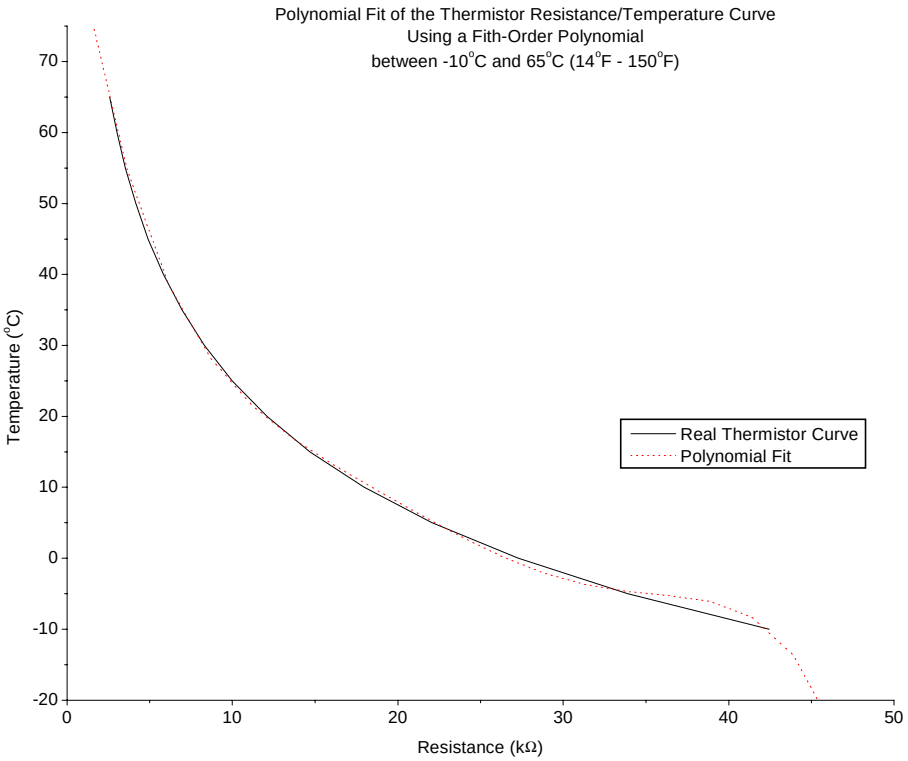

Figure E2. Thermistor Resistance/Temperature Curve

Thermistor available from:

RadioShack Corporation

http://www.radioshack.com

Vita

Thomas Hegewald was born on August 29, 1971 in Dresden, Germany where he spent his childhood and went to school. After graduating from high school, he started a two-year apprenticeship program to become an electrician. Thomas Hegewald began his working career in 1990 in the State Theater of Dresden where he worked as a lighting engineer. In 1995, he decided to go back to school and enrolled in a five-year program at the Dresden University of Technology to earn a diploma in electrical engineering. The student exchange program with Virginia Tech brought him to Blacksburg in 1998 where he was offered to work on a Master's degree in mechanical engineering. After completing the Master's at Virginia Tech in July 2000, Thomas Hegewald plans to go back to Dresden University of Technology to finish his degree in electrical engineering.